Effect of vanadia loading on acidic and redox properties of VO_x/TiO_2 for the simultaneous abatement of PCDD/Fs and NO_x.

M. Gallastegi-Villa, A. Aranzabal*, M.P. González-Marcos, B.A. Markaide-Aiastui, J.A. González-Marcos, J.R. González-Velasco

Group “Chemical Technologies for Environmental Sustainability”

Chemical Engineering Dept., Faculty of Science and Technology

Universidad del País Vasco, UPV/EHU; P.O. Box 644, E-48080 Bilbao, Spain

*E-mail: asier.aranzabal@ehu.es

RESEARCH HIGHLIGHTS

- Effect of vanadia loading on acidic and redox properties of VO_x/TiO_2 is analyzed.
- The role of acidic and redox properties on NOx and o-DCB abatement is analyzed.
- NO SCR reaction occurs mainly on Brønsted type polymeric species.
- o-DCB is adsorbed on Lewis sites associated to monomeric species at low temperature.
- NH_3 and o-DCB compete for Brønsted acid sites at high temperature.

***Graphical Abstract**

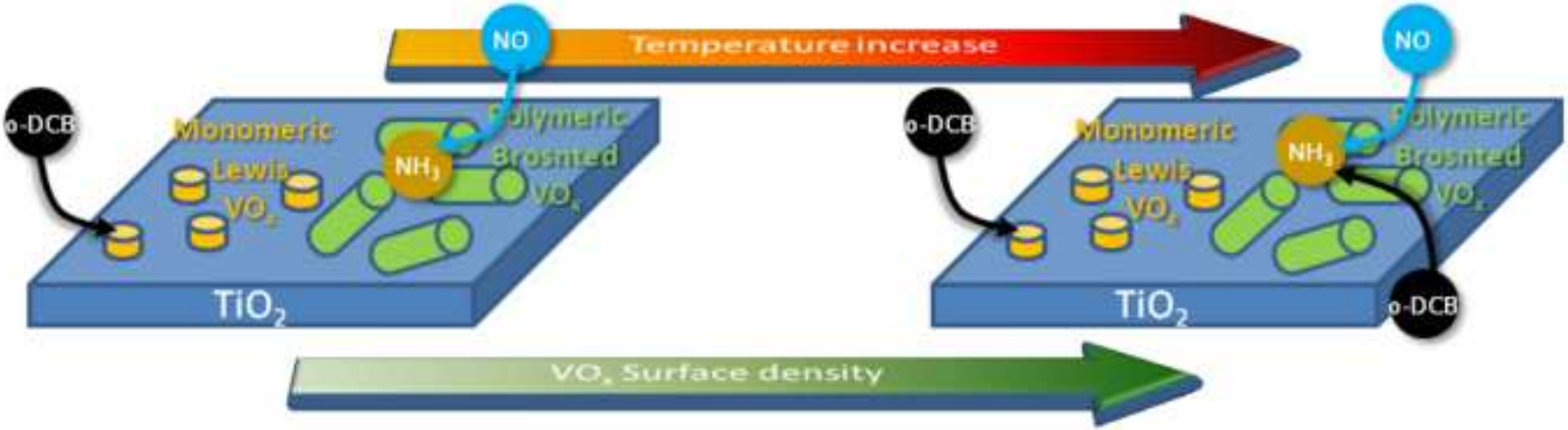

ABSTRACT

The effect of vanadia loading on the acidic and redox properties of VO_x/TiO_2 catalyst and their role in the simultaneous reduction of NO with NH_3 and oxidation of o-DCB is studied. Catalyst samples with different proportions of VO_x species, ranging from monomerics to V_2O_5 octahedral crystals have been prepared. A relationship between VO_x species and their acidic and redox properties was found. At low temperature, o-DCB is adsorbed mainly on Lewis sites, associated to monomeric species, but at high temperature, o-DCB and NH_3 compete for Brønsted sites associated to polymeric species.

Keywords: VO_x/TiO_2, acid, redox, NO, o-dichlorobenzene.

1. INTRODUCTION

Since polychlorinated dibenzo-p-dioxins (PCDDs) and polychlorinated dibenzofurans (PCDFs) were listed and targeted for removal by the Stockholm Convention on Persistent Organic Pollutants (POPs) [1], their emissions from stationary sources have been extensively studied because of their adverse health effects [2]. PCDDs and PCDFs are produced by several industrial operations, but Municipal Solid Waste Incinerators (MSWI) are the major emission sources [2-5]. Several technologies have been developed for PCDD/Fs removal from the flue gas. According to several reviews [2-3,5-6], activated carbon injection followed by bag filter (ACI+BF) is the most widespread technology. High removal efficiencies are reported for this technology, which allows meeting the regulatory limit of 0.1 ng I-TEQ/m^3_N. At times, however, this method can even cause additional dioxin formation. Wet scrubbing may also be considered an effective option for PCDD/Fs abatement, with removal efficiency of 98%. However, adsorption and absorption techniques only transfer dioxins from the gaseous phase to solid or liquid phase. The contaminated adsorbent/absorbent must be subsequently regenerated by thermal treatment at temperatures high enough to destroy the PCDD/Fs or disposed of in an appropriate facility, which represents an additional technical and economic cost. Catalytic filter (CF) technology has been applied in some MSWI. CF technology can simultaneously remove solid- and gas-phase PCDD/Fs without the need of an adsorbent. Hung et al. [7] and Hsu et al. [8] analyzed chlorobenzenes (CBz), chlorophenols (CPh) and PCDDs removal efficiencies using a pilot-scale CF module and compared these with the conventional ACI+BF system. They found lower efficiencies in CBz and CPh removal with CF than with ACI+BF [7], but higher efficiencies for PCDDs removal [8]. Catalytic oxidation is an effective alternative to destroy PCDD/Fs. Haldor Topsøe [9] supplied a DeNOx/CATOX catalytic cleaning unit for a waste incineration plant in Bolzano, Northern Italy. NO_x were firstly reduced (Eq. 1) in DeNOx catalyst with 86% efficiency and subsequently dioxins were oxidized (Eq. 2) in CATOX catalyst with 97% efficiency. According to Goemans et al. [10], 99% of

PCDD/Fs and 90% of NO_x were removed simultaneously (Eq. 1 & 2) over a single and typical $VO_x/WO_x/TiO_2$ DeNOx catalyst at the MSWI plant of Ghent (Belgium). This system requires only minimal additional investment when it is retrofitted to an existing DeNOx unit.

$$4NO + 4NH_3 + O_2 \rightarrow 4N_2 + 6H_2O \quad (1)$$

$$C_{12}H_nCl_{8-n}O_2 + (9+0.5n)O_2 \rightarrow (n-4)H_2O + 12CO_2 + (8-n)HCl \quad (2)$$

Finochio et al. [3] and Du et al. [5] reviewed the behavior of different catalysts for the oxidation of PCDD/Fs. They reported that $VO_x/WO_x/TiO_2$ is superior to supported Pt and Pd and other transition metal oxide catalysts, due to the effect of metal-oxygen interactions. Most laboratory researches have been conducted in conditions of solely oxidation of dioxins [11-16], without simultaneous Selective Catalytic Reduction (SCR) of NO_x, as it would happen within an existing DeNOx unit. Most of these authors use o-dichlorobenzene (o-DCB) as substitute of PCDDs at laboratory scale, due to their handling difficulty and high toxicity [11-12]. In recent years, the catalytic behavior of vanadium-based metal oxide catalysts has been correlated closely to surface acidity and redox ability for different oxidation reactions [17-20]. Vanadia loading is a key point of the catalyst behaviour, as it affects the nature of the VO_x species. Monomeric VO_x species over TiO_2 are reported to be the most active sites for o-DCB oxidation [9-10], the formation of crystalline V_2O_5 being detrimental on oxidation. On the other side, the acidic properties of the catalytic surface have been reported recently to influence the performance of vanadia-based catalyst in total oxidation of o-DCB [21].

There is little literature on simultaneous catalytic removal of NO_x and o-DCB through the combined dDiNOx process. Several authors reported [8,22-23] that NO shows a positive effect on chloroaromatics conversion, likely due to the higher oxidation potential of NO_2 (formed by NO oxidation), which accelerates the redox cycle. Polymeric VO_x species are known to show the highest activity in NO reduction [24-25], and the reaction starts with NH_3 adsorption on Brønsted

acid sites (V-OH). Gallastegui et al. [26-27] found this system was rather complex: a tricky balance for operating conditions must be found, since the normal temperature window of SCR is altered by o-DCB oxidation. Besides, SCR reaction is not efficient above 230 ºC, when the onset of o-DCB oxidation reaction sets in. Thus, temperatures below 230 ºC may ensure very high conversion of NO but very low for o-DCB, whereas higher temperatures (> 350 ºC) may allow high conversion of o-DCB but lower conversion of NO.

Du et al. [5] recently concluded in their review that too little is still known about reaction pathways at the molecular level and the interaction of the different components of the catalyst with the reactants. The aim of this work is to understand comprehensively the relationship among the role of acid and redox sites on the simultaneous NO reduction and o-DCB oxidation on VO_x/TiO_2 catalysts. For this purpose, catalyst samples varying the vanadium loading were prepared so as to obtain samples with different surface densities, ranging from sub-monolayer (below 7.8 V/nm^2) to over-monolayer, which led to different proportions of VO_x species and a broad distribution of acid sites. Reactions of NO reduction and o-DCB oxidation were carried out both simultaneously and separately, at different temperatures. Inlet concentration of co-reactants was also varied.

Due to the complexity of the system, as above stated, water was not included in the feed gas composition at this stage, although it is an important component of combustion gases from MSW incinerators. This issue will be examined in future work based on the results shown in the present paper.

2. EXPERIMENTAL

2.1 Catalyst preparation

Five samples of VO_x/TiO_2 varying the vanadium loading in the range 1-8 wt.% were prepared by wet impregnation. The amount of precursor (NH_4VO_3, Sigma Aldrich, 99,99%) necessary to obtain 1, 1.5, 2.2, 3 and 8 wt.% of vanadium on the final catalyst, was dissolved in distilled water and complexed with 2 moles of oxalic acid (Sigma-Aldrich, 99.99%) per mole of vanadium. The solution was introduced into a Büchi R114 commercial rotary evaporator equipped with a B480 type heating bath and a vacuum system. The solvent was evaporated by maintaining the solution slurry at 35 °C and 0.4 kPa under continuous rotation for 3 h; the resulting samples were dried overnight at 110 °C and then calcined at 500 °C for 3 h (1 °C min^{-1}). As a support, commercial TiO_2 anatase calcined at 520 ºC for 3 h from Millennium Inorganic Chemicals - Cristal Global (Cristal ACTiVTM G5) was used. The catalysts are named as XV/TiO_2, where X is the nominal mass percentage of vanadium: $1V/TiO_2$, $1.5V/TiO_2$, $2.2V/TiO_2$, $3V/TiO_2$ and $8V/TiO_2$.

2.2 Catalyst characterization

The actual amount of metals in the prepared catalysts was determined by ICP-AES (Horiba Jobin Yvon, Activa) after complete dissolution of solid samples in 1:3 HNO_3:HCl mixture followed by a few drops of HF at 90 °C.

Textural properties of catalyst samples were evaluated by means of N_2 adsorption–desorption isotherms at −196 °C in a Micromeritics TRISTAR II 3020 apparatus. The specific surface areas of the prepared samples were determined by the standard BET procedure, using nitrogen adsorption in the relative equilibrium pressure range of 0.03-0.3. Mesopore mean pore size and its distribution were calculated using the BJH method from the desorption branch. The catalyst samples (15-20 mg) were previously degassed under nitrogen flow and under vacuum, respectively, at 350 ºC for 4 h.

Catalysts surface acidity was measured by temperature programmed desorption of NH_3 (NH_3-TPD) performed on a Micromeritics AutoChem 2910 instrument. Prior to adsorption, the samples (15-20 mg) were treated in a quartz U-tube under 5% O_2/He mixture gas flow (50 mL/min) at 500 °C for 45 min, cooled down to 100 °C and treated with helium (50 mL/min) for 60 min. The adsorption step was performed by admitting small pulses of NH_3 in helium (10% NH_3/He) at 100 °C up to saturation. Subsequently, the samples were exposed to a flow of helium (50 mL/min) for 2 h at 100 °C in order to remove reversibly and physically bound NH_3 from the surface. Finally, TPD was started using helium as carrier gas (50 mL/min) from 100 to 550 °C (10 ºC/min) while NH_3 desorption was continuously monitored with a TCD detector. The amount of NH_3 desorbed was determined by time-integrated NH_3-TPD curves as a measure of the acid site concentration.

Redox behavior was examined by temperature programmed reduction using H_2 (H_2-TPR). The experiments were conducted on a Micromeritics AutoChem 2920 instrument. Firstly, all the samples (15-20 mg) were pre-treated under 50 mL/min of 5% O_2/He mixture at 500 °C for 45 min and then cooled down to room temperature and flushed with helium for 60 min. Then, samples were heated from room temperature to 1000 °C (10 °C/min) under a 50 mL/min of 5% H_2/Ar mixture gas flow. The water produced by reduction was removed in a cold trap, and the consumption of H_2 was continuously monitored with a TCD detector. Total H_2 consumption was calculated from time-integrated H_2-TPR curves.

X-ray diffraction (XRD) studies were conducted on a Philips PW 1710 X-ray diffractometer with Cu Kα radiation (λ = 1.5406 Å) and Ni filter. The finely grounded samples were scanned between 10 and 70° (2θ) with 0.02°/s sampling interval. Phase identification was conducted by comparison with JCPDS (Joint Committee on Powder Diffraction Standards) database cards.

The type of surface acidity (Brønsted/Lewis) was determined by pre-absorbing pyridine on the catalyst surface and subsequent desorbing. Transform Infrared (FTIR) spectra of adsorbed pyridine was obtained by a Nicolet Protegé 460 ESP spectrometer, equipped with a Spectra-Tech

high-temperature chamber and nitrogen-cooled MCT detector. All spectra were recorded in the range 4000-50 cm^{-1} averaging 50 scans with 4 cm^{-1} resolution and analyzed using OMNIC software. Prior to adsorption experiments, the samples were treated under 15% O_2/N_2 mixture gas flow (300 cm^3 min^{-1}) at 300 °C for 2 h. Then, they were cooled down to 150 °C under the same atmosphere and the reference background spectra were recorded. Afterwards, pyridine was injected up to saturation. In order to remove reversibly and physically bound pyridine from the surface, the samples were exposed to a flow of N_2 (250 cm^3 min^{-1}) for 1 h. Then, the spectra of adsorbed pyridine were obtained by subtracting the reference spectrum. For high temperature spectra, the reference background was taken at 300 °C and the samples were heated from 150 to 300 °C with a constant heating rate of 10 °C min^{-1} under a flow of N_2 (250 cm^3 min^{-1}). The Brønsted/Lewis (B/L) ratio was calculated as the ratio of the area under the peaks at 1540 cm^{-1} and 1455 cm^{-1} corresponding to pyridine adsorbed on Brønsted and Lewis acid sites, respectively.

Raman spectroscopy was performed in a Raman Olympus spectrometer at the laboratories of Haldor Topsøe S.A in Lyngby. For each spectrum, a 633 nm solid-state laser was used, 30 scans were accumulated in the spectral window from 1400 to 1200 cm^{-1}, and 10 s were employed for each scan. The crushed and sieved (0.05-0.20 mm) samples were introduced in a fluidized reactor. The analyses were performed at 400 °C after sample dehydration at 400 °C for 2 h in air (20 cm^3 min^{-1}).

Diffuse reflectance UV-Vis spectroscopy (UV-Vis) analyses were carried out with a UV-Vis-NIR Cary 5000 apparatus within a range of 200-2500 nm. Prior to the analyses, the samples in powder form were dehydrated in an external oven at 110 °C for 3 h. The repetition of different samples showed high reproducibility of the technique.

2.3 Reaction set-up and catalytic tests.

The experimental reaction set-up consisted of three sections. Firstly, a gas-mixture preparation section formed by a set of mass flow controllers for the individual pure compounds: Bronkhorst® High-Tech F-201CV for gases and a Bronkhorst® High-Tech μ-Flow L01-AAA-99-0-20S for liquid o-DCB. Total evaporation of the liquid stream and homogenous blend with the gas stream was performed in a controlled-evaporator-mixer (Bronkhorst® High-Tech W-102A-111-K). In order to avoid gas adsorption and condensation in the pipes, these were heated with electrical resistances. The composition of the feeding gas mixture was 300 ppm NO, 300 ppm NH_3, 100 ppm o-DCB, 10% O_2, 10% CO_2, and Ar (balance). Secondly, the fixed catalytic bed consisted of 1.5 g of particulate catalysts (0.3-0.5 mm) mixed with inert quartz (0.5-0.8 mm) in order to fill a bed volume of 3 mL, inside a tubular quartz reactor of 13.6 mm internal diameter heated into a convective-flow oven. The nominal gas flow rate was 2 L_N min^{-1}, with a GHSV of 40,000 h^{-1}. Before each catalytic measurement, the fixed bed was dried at 200 ºC for 2 h in pure argon (2 L_N min^{-1}). The reaction temperature was varied from 100 to 500 ºC at a rate of 1.5 °C min^{-1} for some experiments and was kept constant for others. Thirdly, the composition of inlet and outlet gas mixtures was analyzed on line by a GC/MS (Agilent Technologies 7890A/5975C equipped with a HP-VOC capillary column) for o-DCB, and a chemiluminescence analyzer (NGA 200 Rosemount) for NO. NH_3 was only measured at the reactor inlet by trapping in a boric acid solution, and subsequent titration: The feed, without CO_2, was bubbled in a solution of boric acid (0.005 M) for some time, and then the amount of NH_3 reacting with boric acid was determined by measuring the amount of hydrochloric acid solution (0.1 N) required to bring the pH to its initial value. Phenol Red, with a pH range of 6.6 (yellow) - 8.0 (red), was used as an indicator.

Absence of diffusion resistances has been checked by Mear's criterion [28] for external mass transfer ($1.3 \cdot 10^{-2} < 0.15$ for NO reduction at 200 °C and $1.3 \cdot 10^{-2} < 0.15$ for oxidation at 250 °C) and by Weisz-Prater criterion [29] for internal mass transfer ($0.3 < 1$ for NO reduction at 200 °C and $0.2 < 1$ for oxidation at 250 °C). Reproducibility of reaction tests and stability of the catalysts were

analyzed by regularly repeating the same reaction test over a control catalyst sample ($3V/TiO_2$). The standard deviation of NO conversion was below 1.5% in the whole range of temperature, but the standard deviation of o-DCB increased up to 5% in the light-off region.

3.1 Catalyst Characterization

In Table 1, chemical composition and textural and structural properties of prepared VO_x/TiO_2 catalysts are summarized. Final vanadium loadings were confirmed by ICP-AES and used, together with BET surface areas, to estimate vanadium dispersion as surface density (VO_x/nm^2) according to Eq. 3 [30].

$$VO_x/nm^2 = -\frac{x_v \cdot 6.022 \cdot 10^{23}}{MW_V \cdot S_{BET} \cdot 10^{18}} \quad (3)$$

where x_V is the vanadium mass fraction, MW_v is the molecular weight of vanadium in $g \cdot mol^{-1}$ and S_{BET} is the surface area in $m^2 \cdot g^{-1}$.

As expected, $1V/TiO_2$ and $1.5V/TiO_2$ samples are sub-monolayer catalysts since their surface densities (1.83 and 3.50 VO_x/nm^2, respectively) are significantly lower than the monolayer value of ca. 7.8 VO_x/nm^2. Surface densities of $2.2V/TiO_2$ and $3V/TiO_2$ samples (5.31 and 5.89 VO_x/nm^2, respectively) are quite close to the monolayer, whereas $8V/TiO_2$ sample shows by far the highest surface density (25.7 VO_x/nm^2), being an over-monolayer catalyst.

Table 1

BET surface area decreases with vanadium content [16]. High vanadium content ($8V/TiO_2$) produces the formation of crystalline V_2O_5 species, as confirmed by XRD in Fig. 1 [31], which produces an increase of the pore average diameter (d_p) and anatase crystalline size (Table 1).

Fig. 1

VO_x species have been identified by Raman and UV-Vis spectroscopic techniques, Raman being sensitive to V(V) and UV-Vis to V(V) and V(IV). The Raman spectra of support and catalysts are shown in Fig. 2A. With the aim of analyzing the spectral properties of vanadium exclusively, the spectrum of bare TiO_2 has been subtracted from the spectra of VO_x/TiO_2 samples in Fig. 2B.

The numerical integration of those spectra and the vanadium content measured by ICP-AES for sub-monolayer catalysts are linearly dependent (Fig. 3), suggesting that the average oxidation state of vanadium is similar in all catalysts. All samples show a sharp band ca. 1030 cm^{-1}, associated to the V=O stretching mode of dispersed monomeric or polymeric VO_x species, which shifts from 1032 to 1028 cm^{-1} (Fig. 2B) with increasing vanadium loading due to distortions associated with the polymerization of surface monomeric VO_4 species [32-33] when vanadium surface coverage increases. Further vanadium loading leads to crystallization of polymeric species as V_2O_5, according to the sharp vanadyl stretching band at 995 cm^{-1} with low intensity on spectra of 2.2V/TiO_2 and 3V/TiO_2 samples but high intensity on spectrum of 8V/TiO_2 catalyst, in accordance, at least for the 8V/TiO_2 sample, with the XRD results in Fig. 1. The small particle size (<4 nm) and/or concentration of V_2O_5 crystals in 2.2V/TiO_2 and 3V/TiO_2 catalysts made the crystalline species undetectable by XRD [34]. The formation of V_2O_5 crystals is also evidenced by the increase of the Raman band at ca. 680 cm^{-1}.

Fig. 2

Fig. 3

Fig. 2C shows, as an example, the deconvolution of the subtracted bands in Fig. 2B for 3V/TiO2 sample. Polymerization of monomeric species involves the formation of V-O-V in detriment of V-O-s (support) bonds. Although the classical assignment uses the broad Raman band near 930 cm^{-1} as the proof for the presence of polymeric species [33,35-38], theoretical works on VO_x/Al_2O_3 systems suggest that this is a V-O-s bond [39]. Magg et al. [40] also proposed an alternative band assignment for SiO_2 and Al_2O_3 supported VO_x. Thus, the two bands in the range of 950-800 cm^{-1} (Fig. 2B) have been assigned to V-O-Ti and the two bands in the range of 750-650 cm-1 have been assigned to V-O-V in this work. This assignment is consistent with the band position of V-O-V in V_2O_5 crystals (700-750 cm^{-1}) [33], although the identification of these

bands would be hard for V_2O_5/TiO_2 catalysts due to the overwhelming band of anatase at 630 cm^{-1}, which might explain why it has not been reported yet. The bands at lower wavelength (both in V-O-Ti and V-O-V) might be associated to more disperse species (monomeric and polymeric), and those at higher wavelength to less disperse crystalline species, which is consistent with the shift of the bands observed in Fig. 2B.

UV-Vis spectroscopy has been used to verify Raman results and to identify and characterize V(IV) species. Fig. 4 shows the UV-Vis spectra of prepared samples when bare TiO_2 was used as a reference, which allows semi-quantitative analysis [41-43]. Tetrahedral V(V) ligand-to-metal charge transfer (CT) (O →V(V)) transitions are identified as an adsorption band ca. 400 nm, clearly identified by a peak in UV-Vis spectra. The intensity of this band increases with vanadium content because the amount of tetrahedral monomeric and polymeric species increases. Besides that, the red-shift of this band from 392 to 404 nm as vanadium loading increases from 1 to 8 wt.% is likely due to polymerization [42]. At high vanadium loading, tetrahedral polymeric species could be distorted to a square pyramidal structure characterized by a CT band at ca. 440 nm, where both V(V) and V(IV) could coexist. Fig. 4 shows the presence of this band in spectra of $3V/TiO_2$ and $8V/TiO_2$ catalysts. As a consequence, d-d transitions of V(IV) are also observed in all the samples, but primarily in $3V/TiO_2$ and $8V/TiO_2$ around 550 and 668 nm. Finally, CT band of distorted octahedral crystalline species is obtained at ca. 500 nm, noted by a marked shoulder on $8V/TiO_2$ catalyst spectrum and by a light shoulder on $3V/TiO_2$.

Fig. 4

Once the surface VO_x species identified, redox properties of VO_x/TiO_2 catalysts are analyzed since the reducibility is directly related to VO_x species nature. H_2-TPR experiments are shown in Fig. 5 and, although the reduction of all the samples takes place in a single reduction step, the main reduction peak shows different shoulders indicative of the reduction of different species [44]

1V/TiO_2 and 1.5V/TiO_2 catalysts, with low vanadium content in mainly tetrahedral monomeric and polymeric species, present a reduction shoulder at low temperature, indicative of the boundary of the reduction of both species [37]. The reduction profile of 2.2V/TiO_2 sample also fits to two reduction steps, while the profile of 3V/TiO_2 can be deconvolved into three reduction peaks, because of the reduction of small V_2O_5 crystals at higher temperature. The reduction temperature of V_2O_5 crystals matches with the main reduction peak of 8V/TiO_2 sample, which is full of big V_2O_5 particles. Although the reduction profile of crystalline V_2O_5, obtained by thermal decomposition of NH_4VO_3, occurs at higher temperature and in three reduction peaks related to $V^{+5} \rightarrow V^{+4,2} \rightarrow V^{+4} \rightarrow V^{+3}$ reduction stages [25, 45], the absence of more than one reduction peak in the case of 8V/TiO_2 could be explained by heterogeneous distribution of VO_x species and/or smaller particle size of V_2O_5 crystallites, since a V_2O_5 crystallite size of ca. 30 nm has been estimated by XRD for 8V/TiO_2 and ca. 65 nm for the reference V_2O_5.

It is worth noting that the temperature for the maximum reduction rate, identified by the peak, shifts from 422 ºC to 449 ºC as vanadium loading increases from 1 to 3 wt.%, which is indicative of the polymerization process and/or the structural changes. In line with UV-Vis results, further vanadium loading could lead to the formation of square pyramidal species from tetrahedral polymeric species. Thus, the most dispersed species (monomeric), which highly interact with the titanium, are more reducible, followed by polymerics, square pyramidals and V_2O_5 crystals [30,45-46].

Fig. 5

Finally, with the aim to find a relationship between VO_x species and acidic properties, NH_3-TPD and FTIR spectra of adsorbed pyridine are compared in Fig. 6. As Table 1 summarizes, total acidity increases with vanadium loading up to a maximum, which was found to be 332 µmol NH_3/g for 1.5V/TiO_2 sample (3.5 VO_x/nm^2 surface coverage) in agreement with the literature [16,47].

Further loading leads to a gradual decrease of total acidity. The FTIR spectra of adsorbed pyridine (Fig. 6B) reflect that TiO_2 has only Lewis acid sites (1455 cm^{-1}), but the addition of VO_x allows the formation of V–OH, which gives Brønsted acid sites (1540 cm^{-1}) as a result [16,48]. The B/L ratio calculated as the ratio of the area under the peaks at 1540 and 1455 cm^{-1} (Table 1) increases by tenfold when vanadium loading rises from 1 to 8 wt.%. The increase of VO_x surface coverage implies a decrease of VO_x dispersion, which results in lower contribution of V-O-Ti and higher contribution of V-O-V. Therefore, the increase of B/L ratio suggests that the main contribution to Brønsted acidity of VO_x, could be related to oxygen bridge in V-O-V rather than in V-O-Ti.

Fig. 6

A common feature among the samples tested by FTIR is the shift of the Brønsted peak from 1540 to 1536 cm^{-1} with increasing vanadium loading, which could be related to the different strength of the acid sites [26]. In fact, three types of acid strength can be differentiated according to NH_3-TPD profiles (Fig. 6A): weak (100-225 °C), medium (225-350 °C) and strong (350-550 °C). The TiO_2 support mainly shows weak and medium strength acid sites and strong acid sites are generated due to VO_x deposition. Low-vanadium-loading catalysts ($1V/TiO_2$, $1.5V/TiO_2$ and $2.2V/TiO_2$) show a well-defined NH_3 desorption peak at ca. 425 °C, that decreases while vanadium loading increases until disappearing for the $3V/TiO_2$ catalyst. Since it has been concluded that $1V/TiO_2$ sample is rich in monomeric VO_x species, the strongest acid sites could be associated to them. By FTIR measurements [16,48] the strongest acid sites can be confirmed to be Lewis type, since out-gassing at 300 ºC (Fig. 6B, $3V/TiO_2$ sample) affects the intensity of Brønsted acid sites more than that of Lewis acid sites. Therefore, monomeric species show strong and Lewis-type acidity. On the contrary, the acidity of polymeric species, which are predominant in monolayer $3V/TiO_2$ sample, is Brønsted-type and weaker.

3.2 Catalytic performance

Once the nature of VO_x species has been identified and characterized, this section is devoted to analyze their catalytic activity in *dDiNOx* process. Fig. 7 shows the specific activity per vanadium atom in terms of TOF (Turn-Over Frequency) of NO reduction and o-DCB oxidation as a function of VO_x surface density. Eq. 4 has been used for calculating TOF, by assuming the first order reaction accepted in the literature for NO reduction [49-50] and o-DCB oxidation [51-52].

$$TOF = -\frac{F_{A0}\ln(1-X_A)}{P'Wx_v/MW_V} \quad (4)$$

where F_{A0} is reagent entrance molar flow, X_A is reagent conversion, P' is relative pressure, W is catalyst weight, x_v is catalyst vanadium mass fraction and MW_v is vanadium molecular weight.

TOF was measured and calculated at two different temperatures. One at a low temperature (150 or 250 ºC), where the interference of parallel reactions associated mainly to NH_3 oxidation are negligible and the other at a high temperature (300 ºC), where the rate of NH_3 oxidation is significant [53-54], resulting in a lower NO conversion. At 150 ºC, NO reaction rate is considerably high but o-DCB oxidation rate is extremely low, so TOF of o-DCB was measured at 250 ºC. Although NO reaction and o-DCB oxidation are presented in separated graphics in Fig. 7, both reactions were carried out simultaneously feeding 300 ppm of NO and NH_3, 100 ppm of o-DCB and 10% of O_2 and CO_2 to the catalytic reactor.

Fig. 7

The dependency of TOF on VO_x surface density changes with temperature in both reactions, which indicates that the role of VO_x species depends on reaction temperature. At 150 °C, TOF of NO reduction increases up to a maximum near monolayer coverage, where polymeric species concentration is the highest, which confirms their higher activity in NO SCR reaction [24-25]. At further surface density, TOF decreases drastically as a consequence of the low activity of V_2O_5 octahedral crystals in NO SCR. Nonetheless, the TOF of NO reduction decreases at 300 °C

as VO_x surface density increases, not showing a peak at monolayer coverage, which has been associated to active participation of polymeric and crystalline species in NH_3 oxidation reaction [45], adversely competing with NO SCR [53-54], as stated before. The high Brønsted acidity of polymeric species could be related with their high activity [55-56], but not exclusively, because the B/L ratio of the less active 8V/TiO_2 (Table 1), full of big V_2O_5 particles, is even higher. However, the reducibility of V_2O_5 in 8V/TiO_2 is considerably lower in comparison with the polymeric species (3V/TiO_2) as measured by H_2-TPR (Fig. 5). Then, the balanced combination of Brønsted acidity and high reducibility together with the type of structure of polymeric species with adjacent vanadium atoms, explains the TOF peak of 3V/TiO_2 at 150 ºC. Some authors [25,33] suggest that the superiority of polymeric species is due to the dual-site Eley-Rideal mechanism [53,57-58]. This reaction mechanism involves two vanadium sites: a surface vanadia redox site and an adjacent non-reducible acid site.

The kinetic data obtained in the *dDiNOx* reaction system and analyzed in the following paragraphs support the hypothesis that more than one surface VO_x site may be involved in the rate-determining step of NO reduction. The linear relationship found in Fig. 3 between the number of surface VO_x species and the vanadium loading in the sub-monolayer region, allows for the quantitative determination of the number of surface active sites involved in the rate determining step as suggested by Zaho and Wachs [38] for propylene selective oxidation over supported vanadium oxide catalysts. For this purpose, the kinetic expression for the rate of NO SCR reaction can be expressed as a function of surface VO_x density, as:

$$-r_A = \frac{dX_A}{d\left(W/F_{A0}\right)} = kC_A^a C_B^b \left[VO_x/nm^2\right]^n \quad (5)$$

For constant partial pressures of the reactants, temperature and flow rates, Eq. 5 can be further simplified and linearized as:

$$\ln\left(\frac{-F_{A0}\ln(1-X_A)}{PC_{A0}W}\right)=\ln(k')+n\ln\left(\left[VO_x/nm^2\right]\right) \quad (6)$$

where *k*' is the product of constant parameters, including rate constants and a function of reactants concentration. The exponent *n* can be readily determined from the slope of the plot of: ln[-r_A (mol NO/(g s))] vs. ln[VO_x/nm^2], as shown in Fig. 8. The plot includes experimental data of this work and data from literature on NO SCR over VO_x/TiO_2 catalysts [24-25,59]. Fitting straight lines to data resulted in a value of the slope between 2.0 and 2.4, which confirms the participation of two vanadium atoms in the SCR reaction [25,33]. Since plotted literature data were obtained in the absence of o-DCB oxidation, unlike current data, o-DCB oxidation seems to produce very little effect on NO reduction.

Fig. 8

The superior activity of polymeric species in NO SCR is also confirmed by Fig. 9, in which calculated apparent activation energy has been represented versus VO_x surface density. The apparent activation energy was calculated by the linear regression of Arrhenius plot derived from Eq. 7. The coefficient of determination of the linear fit was always higher than 0.997.

$$\ln\left(\frac{-F_{A0}\ln(1-X_A)}{PC_{A0}W}\right)=\ln(k_0)-\frac{Ea}{RT} \quad (7)$$

It can be seen that the highest value of apparent activation energy is obtained with $1V/TiO_2$, and decreases drastically to the lowest value for $3V/TiO_2$. Interestingly, the obtained trend is inversely related to the TOF (Fig. 7A). Thus, it can be suggested that the activation of NH_3 adsorbed on a Brønsted acid site through an adjacent redox site [58], and/or the reoxidation of the redox site, are likely to accelerate in polymerics due to the proximity of the two vanadium atoms.

The decrease of apparent activation energy with vanadium loading has already been reported by Amiridis and Solar [60] in dry conditions and in the presence of SO_2.

FIG. 9

Comparable values of activation energy in the range of 40-60 kJ/mol are reported in the literature for the SCR reaction with VO_x/TiO_2 catalyst [49-50,61]. Tronconi et al. [57] found an activation energy of 94 kJ/mol for commercial SCR catalyst, in reasonable agreement with the present results since commercial SCR catalyst usually contains low amount of VO_x (ca.1 wt.%) [62]. The high activation energy of $1V/TiO_2$ could be also associated to the shortage of Brønsted type acid sites (B/L=0.07) and consequent adsorption of NH_3 on Lewis type acid sites [43,63]. Then, we can figure out that the first step of NO SCR reaction is the adsorption of NH_3 on Brønsted acid site (V-OH), followed by its activation via redox by reducing the adjacent V(V) to V(IV) (V=O) and the final reaction between activated NH_3 and gas phase or weakly adsorbed NO.

Regarding o-DCB oxidation, the evolution of TOF with VO_x surface density is completely different to that for NO. There is also a slightly different behavior at low (250 ºC) and high (300 ºC) temperature, as shown in Fig. 7B. At the former, TOF decreases with VO_x surface coverage, which indicates that monomeric species are more active [14-15] than polymeric and crystalline species. Conversely, at higher temperature (300 °C) the TOF keeps almost constant up to monolayer coverage (7.8 VO_x/nm^2) and then decreases drastically, which reflects that polymeric [64] species are as active as monomeric species, but crystalline species are definitely less active, both at low and high temperature. These results indicate that o-DCB is more easily adsorbed and oxidized over monomeric species due to their higher reducibility and higher Lewis-type acidity as determined in section 3.1. Gannoun et al. [15] also found that the most dispersed monomeric species are the most reducible and, consequently, the most active species. Krishnamoorthy et al.

[14] observed a decrease of TOF with increasing vanadium content. The reported TOF values (around 10^{-3} s^{-1}) were comparable to those presented in Fig. 7B. Schimmoeller et al. [64] concluded that V-O-V bonds sitting directly on the anatase are the most active bonds for o-DCB oxidation.

Due to the higher proportion of Lewis sites compared to Brønsted sites in samples with higher population of monomeric VO_x species, like in $1V/TiO_2$ (Table 1), at low temperature their high activity can be associated to Lewis acid sites, on which a weak and reversible interaction with o-DCB, through nucleophilic substitution of C-Cl bond on V=O species to form surface phenolate species, is most likely (Fig. 8A), as reported Larrubia and Busca [65], Lichtenberger and Amiridis [66], Wang et al. [67] and Xu et al.[13].

FIG. 10

In order to support this conclusion, the number of surface active sites involved in the rate-determining step of o-DCB oxidation was calculated following the same procedure presented some paragraphs above for NO reduction with NH_3 (Fig. 8). Unfortunately, the o-DCB oxidation rate data collected in this work cannot be used because of the big effect of NO and NH_3 co-feeding, as will be discussed below. Alternatively, the literature data of chlorobenzene oxidation without the presence of NO SCR [14,64,67] was used to calculate logarithmic relation between o-DCB oxidation rate and surface density. The three fitting lines yield slopes of n=0.6-0.9, which can be rounded to the participation of one vanadium atom in o-DCB oxidation. This result is consistent with the assertion that dispersed monomeric species (Lewis acid sites) are mainly involved in o-DCB oxidation.

FIG. 11

Although Brønsted type is lower than Lewis type acidity, we found evidences that the role of the Brønsted acidity, associated mainly to polymeric VO_x species, is also relevant especially in

samples with high vanadium loadings, such as 3V/TiO_2 and 8V/TiO_2, and at high temperature. Table 1 shows the peak concentration of dichloromaleic anhydride (DCMA) measured in the catalytic test of *dDiNOx* reaction. The formation of this type of chlorinated aromatic intermediates suggests that adsorption of o-DCB occurs through the carbon substituted with hydrogen [68-69], instead of through chlorine, as illustrated in Fig. 10B. Like Albonetti et al. [16], a direct relationship between DCMA concentration and Brønsted acidity has been found, beside the nucleophilic attack on the chlorine position proposed by many authors [13,65-67]. Taralunga et al. [68] reported, over zeolites, that the first o-DCB molecule could directly react with the protonic Brønsted acid site, giving HCl, while the second o-DCB could react with the first molecule to give chlorobenzene and dichlorinated adsorbed species. Then, DCMA can be consequently formed from the reaction between this chemisorbed intermediate and oxygen, in a similar way to the formation of maleic anhydride from benzene oxidation over V_2O_5/MoO_3. Weber and Sakurai [69] suggested that hydrogen abstraction was the preferred step, whereas the initial abstraction of chlorine was only a minor pathway on TiO_2-based V_2O_5/WO_3 catalyst, on the basis of their experiments on the oxidation of selected individual PCB isomers and on the isomer specific analysis of PCDF formed. No DCMA was detected with low or medium loading catalysts (1V/TiO_2 to 2.2V/TiO_2), except some traces in the latter. However, notable concentration, around 20 ppm, was monitored in the case of monolayer (3V/TiO_2) and significantly higher amount, ca. 55 ppm, was quantified in the presence of over-monolayer catalyst (8V/TiO_2). Maleic anhydride production was also detected on 8V/TiO_2 sample, whose formation also suggests that adsorption of o-DCB occurs through the carbon substituted with hydrogen. The adsorption of o-DCB on Brønsted acid sites at high temperature is also confirmed by the inhibitory effect of NH_3 on o-DCB conversion discussed below.

The participation of Brønsted acidity in higher vanadium loaded samples and at high temperature is also evidenced by comparing the apparent activation energies. Figure 12 shows the Arrhenius plot assuming the first order reaction (Eq. 7) [14,52]. Over 1V/TiO_2 the Arrhenius plot

shows a linear trend in the whole range of temperature (100–500 °C) but, in the case of higher loaded samples, three zones could be differentiated: low, medium and high temperature. Only data at the medium range (between 180 and 350 °C) have been used for linear regression. The lower slope in the high temperature range (> 350 °C) is common when mass transfer controls the reaction rate [70]. The absence of mass transfer limitation over $1V/TiO_2$ is probably due to its high specific area and pore volume (Table 1) and lower reaction rate.

FIG. 12

Figure 12B shows there is a marked difference between the activation energy of $1V/TiO_2$ (24.5 kJ/mol) and the samples close to monolayer coverage, $1.5\text{-}3V/TiO_2$, with a similar value around 40 to 50 kJ/mol, which agree with data in the literature [67]. This fact confirms the difference in chlorobenzene adsorption over pure Lewis-type monomeric VO_4 species and Brønsted and Lewis-type polymeric VO_x species. Krishnamoorthy et al. [14] also obtain similar values of the activation energy in the range 40-55 kJ/mol varying the vanadium loading over Al_2O_3 in the range of 30-60% of the monolayer. Further vanadium loading leads to slightly higher activation energy, which confirms the lower activity of V_2O_5 particles.

In order to get a clearer picture and confirm the effect of the different nature of active sites on NO, NH_3 and o-DCB adsorption and reaction discussed above, further experiments were carried out by analyzing the catalytic behavior in NO reduction in the absence and in the presence of o-DCB oxidation and vice versa. $3V/TiO_2$ catalyst was selected for these experiments because it contains both monomeric and polymeric VO_x species and both Lewis and Brønsted acid sites. Fig. 13A confirms the small effect of the presence of o-DCB and its oxidation on NO conversion while Fig. 13B and C show a big effect of the presence of NO and NH_3 on o-DCB oxidation. According to Fig. 13C, excess NH_3 hardly affects NO conversion at 150 ºC because no o-DCB oxidation occurs in those conditions and there is enough NH_3 to react with NO according to Eq. 1. However, at 250

°C, NO conversion raised from 54 to 100% when the NH_3/NO ratio varied from sub-stoichiometric (0.8) to super-stoichiometric (1.9) feeding, because competitive reactions, such as NH_3 oxidation, consume NH_3 and, consequently, NO conversion is limited by NH_3 concentration [25,53]. On the other hand, according to Fig. 93B, the increase of NO inlet concentration from 0 to 300 ppm leads to a notable increase of o-DCB conversion from 20 to 60%, which confirms that NO is not competing with o-DCB for neither monomeric nor polymeric species, since it reacts from the gas phase with adsorbed NH_3 preferably on Brønsted-type polymeric species. Some authors suggested that the presence of NO_2 (formed by NO oxidation) can (i) accelerate the vanadium re-oxidation stage [13,22-23] and/or (ii) activate surface oxygen species accelerating the oxidation of the aromatic ring [71-72]. Concentration of NO above 300 ppm does not seem to further improve o-DCB conversion, in agreement with the results of Xu et al. [13], low amount of NO_2 being enough to accelerate o-DCB oxidation rate-limiting stage.

Hence, in line with previous results, the rate-limiting stage in o-DCB oxidation at low temperature can be concluded to be a redox stage, Lewis type monomeric species being the most reducible and, therefore, the most active sites. On the contrary, the increase of NH_3 concentration, noted as NH_3/NO ratio in Fig. 9C, leads to a drastic decrease of o-DCB conversion [13], from 68 to 19% when the NH_3/NO ratio varies from 0.8 to 1.9. Thus, the lower o-DCB conversion is explained by the competition between NH_3 and o-DCB for the same Brønsted acid sites, which confirms the participation of Brønsted-type polymeric species on o-DCB oxidation over $3V/TiO_2$.

FIG. 13

4. CONCLUSIONS

This research work was focused on understanding the role of acidic and redox properties of VO_x/TiO_2 catalyst on the simultaneous NO reduction and o-DCB oxidation, namely *dDiNOx* process. Catalyst samples with different proportions of VO_x species, ranging from monomerics to V_2O_5 octahedral crystals, have been prepared and characterized, and their catalytic behavior was tested both on simultaneous and independent abatement of NO and o-DCB.

The polymerization of isolated species and the formation of square pyramidal species and octahedral crystalline V_2O_5 particles increases as VO_x surface density is increased. Over monolayer catalysts small crystallites are already formed, but two-dimensional tetracoordinate polymerics and square pyramidal are the most abundant species, which leads to reduce the average vanadium oxidation state. Monomerics are the most reducible species and Lewis-type strong acidic centers. Contrarily, polymerics and crystallites are more resistant to reduction and their acidic nature is weaker and mainly Brønsted type.

A relationship between activity of VO_x species, their reducibility and acidity has been found. NO reduction takes place at lower temperature than o-DCB oxidation. Isolated tetracoordinate VO_4 monomeric species, formed at low vanadium loadings, produce strong, Lewis-type acidic sites, which lead to fast o-DCB adsorption and consequently high TOF for o-DCB oxidation. The reducibility of isolated monomeric species is the highest, so the nucleophiles to attack the chlorine position of adsorbed o-DCB molecule occur easily. The rate of o-DCB oxidation over catalyst with high VO_x surface density at low temperature is lower because larger VO_x species, such as polymerics, square pyramidal structures and crystalline particles show worse acidic properties in terms of capacity and strength. The reducibility of the less dispersed species is also lower, probably due to less interaction with the TiO_2 support. In this case, the adsorption of o-DCB occurs

through the carbon substituted with hydrogen, instead of through chlorine, which leads to the formation of intermediate species such as dichloromaleic anhydride and maleic anhydride.

Contrarily, the less dispersed polymeric and square pyramidal species have been found to be the most active for SCR of NO, which involves two vanadium sites acting as adjacent redox and Brønsted acid sites for the adsorption of NH_3. Then, NO reduction is little affected by the presence of o-DCB because it is mainly adsorbed over monomeric species and also because SCR reaction takes place (without parallel reaction) at low temperature, at which the rate of o-DCB oxidation is still low. However, by using samples with higher VO_x surface density and even at higher temperature, there is a competition between o-DCB and NH_3 for polymeric species which leads to lower o-DCB conversion in the presence of SCR of NO as in *dDiNOx* process.

5. ACKNOWLEDGMENTS

This research was funded by Basque Government though the Grant to Consolidated Research Groups (GIC-07/67-JT-450-07) and the SAIOTEK program (S-PE11UN074), by University of the Basque Country (UPV/EHU) through the UFI (UFI 11/39) and the Grant for the acquisition and renovation of scientific infrastructure (INF12/37) and by the Spanish Ministry of Economy and Competitiveness (CTM2012-31576 and CTQ2015-64616-P/MINECO/FEDER). One of the authors (M. Gallastegi-Villa) acknowledges also the Basque Government for the PhD Research Grant (BFI-2011-238). The authors would also like to thank the technical and human support from UPV/EHU Advanced Research Facilities (SGIker) in XRD, ICP, UV-vis, and Haldor Topsøe A/S (S.B. Rasmussen) in Raman. Millennium Inorganic Chemicals – Cristal Global is also acknowledged for kindly supplying TiO_2 (CristalACTiV™ G5).

REFERENCE LIST

[1] Stockholm Convention, http://chm.pops.int/

[2] Y. Peng, J. Chen, S. Lu, J. Huang, M. Zhang, A. Buekens, X. Li, J. Yan, Chem. Eng. J. 292 (2016) 398-414. https://doi.org/10.1016/j.cej.2016.01.102.

[3] E. Finocchio, G. Busca, M. Notaro. Appl. Catal. B: Environ. 62, (2006) 12-20. https://doi.org/10.1016/j.apcatb.2005.06.010.

[4] G. Wielgosiński, Int. J. of Chem. Eng. 2010 (2010) 1-11. https://doi.org/10.1155/2010/392175.

[5] C. Du, S. Lu, Q. Wang, A. G. Buekens, M. Ni, D. P. Debecker. Chem. Eng. J. 334 (2018) 519-544. https://doi.org/10.1016/j.cej.2017.09.018.

[6] A. Mukherjeea, B. Debnathb, S. K. Ghosh. Procedia Environ. Sci. 35 (2016) 528 – 540. https://doi:10.1016/j.proenv.2016.07.037.

[7] P. C. Hung, S. H. Chang, M. B. Chang. Aerosol Air Qual. Res. 14 (2014) 1215–1222.

[8] W. T. Hsu, P. C. Hung, M. B. Chang. Waste Manag. 46 (2015) 257–264.

[9] A. B. Jensen, H. Jensen-Holm, M. Schröter, Catalytic removal of NOx, VOC and dioxin. Haldor Topsøe A/S., Originally presented at Pollutec 2000, October 17-20, Lyon, France. https://www.topsoe.com/file/topsoecatalyticnoxremovalashxpdf-0.

[10] M. Goemans, P. Clarysse, J. Joannès, P. De Clercq, S. Lenaerts, K. Matthys, K. Boels. Chemosphere 54 (2004) 1357–1365.

[11] F. Bertinchamps, C. Grégoire and E.M. Gaigneaux, Appl. Catal., B. 66 (2006) 1-9. https://doi.org/10.1016/j.apcatb.2006.02.011.

[12] E. Finocchio, G. Ramis, G. Busca, Catal. Today 169 (2011) 3-9. https://doi.org/10.1016/j.cattod.2010.10.097.

[13] Z. Xu, S. Deng, Y. Yang, T. Zhang, Q. Cao, J. Huang, G. Yu, Chemosphere 87 (2012) 1032-1038. https://doi.org/10.1016/j.chemosphere.2012.01.004.

[14] S. Krishnamoorthy, J.P. Baker, M.D. Amiridis, Catal. Today 40 (1998) 39-46. https://doi.org/10.1016/S0920-5861(97)00117-X.

[15] C. Gannoun, R. Delaigle, P. Eloy, D.P. Debecker, A. Ghorbel, E.M. Gaigneaux, Catal. Commun.15 (2011) 1-5. https://doi.org/10.1016/j.catcom.2011.08.001.

[16] S. Albonetti, S. Blasioli, R. Bonelli, J.E. Mengou, S. Scirè, F. Trifirò, Appl. Catal. A. 341 (2008) 18-25. https://doi.org/10.1016/j.apcata.2007.12.033.

[17] G. Sui, Z. Xue, D. Zhou, Y. Wang, S. Zhu. J. Ind. Eng. Chem., 51 (2017) 229-236. http://doi.org/10.1016/j.jiec.2017.03.006.

[18] H. Zhao, S. Bennici, J. Cai, J. Shen, A. Auroux, Catal. Today 152 (2010) 70-77. http://doi.org/10.1016/j.cattod.2009.08.005.

[19] M. Xue, G, Jiahen, H. Zhang, J. Shen. Mol. Catal. 330 (2007) 117-126. http://doi.org/10.1016/j.apcata.2007.07.014

[20] A. Ko, Y. Woo, J. Jang, Y. Jung, Y. J. Lee. J. Ind. Eng. Chem., 78 (2019) 433-439. https://doi.org/10.1016/j.jiec.2019.05.024.

[21] M. Gallastegi-Villa, A. Aranzabal, J.A. González-Marcos, J.R. González-Velasco, Appl. Catal., B. 205 (2017) 310-318. https://doi.org/10.1016/j.apcatb.2016.12.020

[22] G. Su, Catal. Sci. Technol. 5 (2015) 1041-1051. https://doi.org/10.1039/C4CY01194E

[23] F. Bertinchamps, M. Treinen, N. Blangenois, E. Mariage, E.M. Gaigneaux, J. Catal. 230 (2005) 493-498. https://doi.org/10.1016/j.jcat.2005.01.009

[24] F. Tang, K. Zhuang, F. Yang, L. Yang, B. Xu, J. Qiu, Y. Fan, Chinese J. Catal. 33 (2012) 933-940. https://doi.org/10.1016/S1872-2067(11)60365-3.

[25] I.E. Wachs, G. Deo, B.M. Weckhuysen, A. Andreini, M.A. Vuurman, M.d. Boer, M.D. Amiridis, Selective Catalytic Reduction of NO with NH_3 over Supported Vanadia Catalysts, J. Catal 161 (1996) 211-221.

[26] M. Gallastegi-Villa, A. Aranzabal, Z. Boukha, J.A. González-Marcos, J.R. González-Velasco, M.V. Martínez-Huerta and M.A. Bañares, Catal. Today 254 (2015) 2-11. https://doi.org/10.1016/j.cattod.2015.02.029

[27] M. Gallastegi-Villa, A. Aranzabal, J.A. González-Marcos, J.R. González-Velasco, Appl. Catal., B. 184 (2016) 238-245. https://doi.org/10.1016/j.apcatb.2015.11.006

[28] D.E. Mears, Tests for Transport Limitations in Experimental Catalytic Reactors, Ind. Eng. Chem. Prod. 10 (1971) 541-547.

[29] P.B. Weisz , C.D. Prater, Interpretation of measurements in experimental catalysis, Adv. Catal. 6 (1954) 143-196.

[30] I.E. Wachs, B.M. Weckhuysen, Appl. Catal., A. 157 (1997) 67-90. https://doi.org/10.1016/S0926-860X(97)00021-5

[31] J. Choi, C.B. Shin, T. Park, D.J. Suh, Appl. Catal. A. 311 (2006) 105-111. https://doi.org/10.1016/j.apcata.2006.06.030.

[32] T. Kim, I.E. Wachs, J. Catal. 255 (2008) 197-205. https://doi.org/10.1016/j.jcat.2008.02.007

[33] I. Giakoumelou, C. Fountzoula, C. Kordulis, S. Boghosian, J. Catal. 239 (2006) 1-12. https://doi.org/10.1016/j.jcat.2006.01.019.

[34] P. Gallezot, X-Ray techniques in catalysis, Catalysis, science and technology, J.R. Anderson, M. Boudart (Eds.), Springer-Verlag, Berlin, 1984.

[35] E.I. Ross-Medgaarden, I.E. Wachs, J. Phys. Chem. C. 111 (2007) 15089-15099. https://doi.org/10.1021/jp074219c.

[36] R. Bulánek, P. Čičmanec, H. Sheng-Yang, P. Knotek, L. Čapek, M. Setnička, Appl. Catal. A. 415–416 (2012) 29-39. https://doi.org/10.1016/j.apcata.2011.11.033.

[37] D.A. Bulushev, L. Kiwi-Minsker, F. Rainone, A. Renken, J. Catal. 205 (2002) 115-122. https://doi.org/10.1006/jcat.2001.3427.

[38] C. Zhao, I.E. Wachs, J. Catal. 257 (2008) 181-189. https://doi.org/10.1016/j.jcat.2008.04.022

[39] V. Brázdová, M. V. Ganduglia-Pirovano, J. Sauer, J. Phys. Chem. B,. 109 (2005) 23532-23542. https://doi.org/10.1021/jp0539167

[40] N. Magg, B. Immaraporn, J.B. Giorgi, T. Schroeder, M. Bäumer, J. Döbler, Z. Wu, E. Kondratenko, M. Cherian, M. Baerns, P.C. Stair, J. Sauer, H. Freund, J. Catal. 226 (2004) 88-100. https://doi.org/10.1016/j.jcat.2004.04.021

[41] H. Berndt, A. Martin, A. Brückner, E. Schreier, D. Müller, H. Kosslick, G.-. Wolf, B. Lücke, J. Catal. 191 (2000) 384-400. https://doi.org/10.1006/jcat.1999.2786

[42] D. Srinivas, W.F. Hölderich, S. Kujath, M.H. Valkenberg, T. Raja, L. Saikia, R. Hinze, V. Ramaswamy, J. Catal. 259 (2008) 165-173. https://doi.org/10.1016/j.jcat.2008.07.019.

[43] D.W. Kwon, K.H. Park, S.C. Hong, Appl. Catal. A. 499 (2015) 1-12. https://doi.org/10.1016/j.apcata.2015.04.005

[44] M.V. Martínez-Huerta, J.L.G. Fierro, M.A. Bañares, Catal. Commun. 11 (2009) 15-19. https://doi.org/10.1016/j.catcom.2009.08.002.

[45] S. Besselmann, C. Freitag, O. Hinrichsen, M. Muhler, Phys. Chem. Chem. Phys. 3 (2001) 4633-4638. https://doi.org/10.1039/B105466J

[46] G.C. Bond, Preparation and properties of vanadia/titania monolayer catalysts, Appl. Catal. A. 157 (1997) 91-103.

[47] Y. Habuta, N. Narishige, K. Okumura, N. Katada, M. Niwa, Catal. Today. 78 (2003) 131-138. https://doi.org/10.1016/S0920-5861(02)00313-9

[48] C. Lin, H. Bai, Appl. Catal. B. 42 (2003) 279-287. https://doi.org/10.1016/S0926-3373(02)00240-0

[49] B.K. Yun, M.Y. Kim, Appl. Therm. Eng. 50 (2013) 152-158. https://doi.org/10.1016/j.applthermaleng.2012.05.039.

[50] L. Lietti, I. Nova, E. Tronconi, P. Forzatti, Catal. Today 45 (1998) 85-92. https://doi.org/10.1016/S0920-5861(98)00253-3.

[51] S. Krishnamoorthy, J.A. Rivas, M.D. Amiridis, J. Catal. 193 (2000) 264-272. https://doi.org/10.1006/jcat.2000.2895.

[52] G. Wielgosiński, A. Grochowalski, T. Machej, T. Pająk, W. Ćwiąkalski, Chemosphere. 67 (2007) 150- https://doi.org/154. 10.1016/j.chemosphere.2006.05.097

[53] G. Busca, L. Lietti, G. Ramis, F. Berti, Appl. Catal., B. 18 (1998) 1-36. https://doi.org/10.1016/S0926-3373(98)00040-X.

[54] R.M. Heck, Catal. Today. 53 (1999) 519-523. https://doi.org/10.1016/S0920-5861(99)00139-X

[55] C. Sun, L. Dong, W. Yu, L. Liu, H. Li, F. Gao, L. Dong, Y. Chen, J. Mol. Catal. A: Chem. 346 (2011) 29-38. https://doi.org/10.1016/j.molcata.2011.06.004.

[56] E. Broclawik, A. Góra, M. Najbar, J. Mol. Catal. A: Chem. 166 (2001) 31-38. https://doi.org/10.1016/S1381-1169(00)00462-3.

[57] E. Tronconi, I. Nova, C. Ciardelli, D. Chatterjee, M. Weibel, J. Catal. 245 (2007) 1-10. https://doi.org/10.1016/j.jcat.2006.09.012.

[58] N.Y. Topsoe, Science. 265 (1994) 1217-1219. https://doi.org/10.1126/science.265.5176.1217

[59] P.G.W.A. Kompio, A. Brückner, F. Hipler, G. Auer, E. Löffler, W. Grünert, J. Catal. 286 (2012) 237-247. https://doi.org/10.1016/j.jcat.2011.11.008.

[60] M. D. Amiridis, J. P Solar, Ind. Eng. Chem. Res. 35 (1996) 978-981. https://doi.org/10.1021/ie950452y.

[61] N. Topsøe, T. Slabiak, B.S. Clausen, T.Z. Srnak, J.A. Dumesic, J. Catal. 134 (1992) 742-746. https://doi.org/10.1016/0021-9517(92)90358-O.

[62] L.J. Alemany, F. Berti, G. Busca, G. Ramis, D. Robba, G.P. Toledo, M. Trombetta, Appl. Catal. B: Environ. 10 (1996) 299-311. https://doi.org/10.1016/S0926-3373(96)00032-X

[63] S. Moon Lee, S. Su Kim, S. Chang Hong, Chem. Eng. Sci. 79 (2012) 177-185. https://doi.org/10.1016/j.ces.2012.05.032

[64] B. Schimmoeller, R. Delaigle, D.P. Debecker, E.M. Gaigneaux, Catal. Today 157 (2010) 198-203. https://doi.org/10.1016/j.cattod.2010.01.029.

[65] M.A. Larrubia, G. Busca, Appl. Catal., B. 39 (2002) 343-352. https://doi.org/10.1016/S0926-3373(02)00116-9.

[66] J. Lichtenberger, M.D. Amiridis, J. Catal. 223 (2004) 296-308. https://doi.org/10.1016/j.jcat.2004.01.032.

[67] J. Wang, X. Wang, X. Liu, J. Zeng, Y. Guo, T. Zhu, J. Mol. Catal. A: Chem. 402 (2015) 1-9. https://doi.org/10.1016/j.molcata.2015.03.003.

[68] M. Taralunga, J. Mijoin, P. Magnoux, Catal. Commun. 7 (2006) 115–121.

[69] R. Weber, T. Sakurai, Appl. Catal., B. 34 (2001) 113-127. https://doi.org/10.1016/S0926-3373(01)00211-9

[70] F. Duprat, Chem. Eng. Sci. 57 (2002) 901-911. https://doi.org/10.1016/S0009-2509(01)00409-2.

[71] G.Centi, F. Cavani, F.Trifirò, Selective Oxidation by Heterogeneous Catalysis, First edi. Kluwer Academic (Eds.), Nueva York, 2001.

[72] E.V. Kondratenko, O. Ovsitser, J. Radnik, M. Schneider, R. Kraehnert, U. Dingerdissen, Appl. Catal., A. 319 (2007) 98-110. https://doi.org/10.1016/j.apcata.2006.11.021

TABLE AND FIGURE CAPTIONS

Table 1: VO_x/TiO_2 catalysts characterization results.

Fig. 1: XRD diffractograms of VO_x/TiO_2 catalysts.

Fig. 2: A) Raman spectra and B) TiO_2 subtracted Raman spectra of VO_x/TiO_2 catalysts. C) Deconvolution of $3VO_x/TiO_2$ sample TiO_2 subtracted Raman spectrum.

Fig. 3: ICP vs. TiO_2 subtracted Raman spectra integration.

Fig. 4: UV-Vis spectra of VO_x/TiO_2 catalysts using TiO_2 as a background.

Fig. 5: H_2-TPR profiles VO_x/TiO_2 catalysts.

Fig. 6: The acidic properties of VO_x/TiO_2 catalysts. A) NH_3-TPD and B) FTIR of adsorbed pyridine.

Fig. 7: TOF of A) NO reduction and B) o-DCB oxidation at different temperatures (100 ppm o-DCB, 300 ppm NO, 300 ppm NH_3, 10 % O_2, 10% CO_2, 2 L_N min^{-1}, 1.5 atm and 80 L_N $(h\ g)^{-1}$).

Fig. 8: $\ln(-r_A)$ vs. $\ln(VO_x)$ of activity data from this work and literature [14-15, 49] in NO reduction and over monolayer VO_x/TiO_2 catalysts.

Fig. 9: Apparent activation energy as a function of VO_x surface density over VO_x/TiO_2 catalysts. Apparent activation energies were calculated by linear regression of $\ln[F_{A0}\cdot\ln(1-x_A)/(P\cdot C_{A0}\cdot W)]$ vs 1/T.

Fig. 10: Adsorption mechanism of o-DCB on A) Lewis and B) Brønsted acid sites.

Fig. 11: $\ln(-r_A)$ vs. $\ln(VO_x)$ calculated from literature in chlorobenzene oxidation and over VO_x/TiO_2 catalysts [8, 54, 57].

Fig. 12: A) Arrhenius plot in o DCB oxidation over VO_x/TiO_2 catalysts and B) apparent activation energy as a function of VO_x surface density.

Fig. 93: Effect of A) o-DCB feed concentration B) NO feed concentration C) NH_3/NO feed ratio on NO and o-DCB conversion ($3V/TiO_2$, 100 ppm o-DCB, 300 ppm NO, 400 ppm NH_3, 2 L_N min^{-1}, 1.5 atm and 80 L_N $(h\ g)^{-1}$).

Table 1: VOx/TiO2 catalysts characterization results.

Sample	V, wt.%	Surface density, VO_x/nm^2	S_{BET}, m^2/g	d_p, nm	Anatase crystal, nm	Total acidity, μmol NH_3/g	B/L	DCMA (temperature), ppm (ºC)
TiO_2	---	---	70	14.6	24	165	0.00	
$1V/TiO_2$	1.05	1.83	68	12.7	23	309	0.07	-
$1.5V/TiO_2$	1.60	3.50	54	15.6	21	332	0.05	-
$2.2V/TiO_2$	2.20	5.31	49	16.0	23	254	0.25	-
$3V/TiO_2$	2.94	5.89	59	12.8	26	229	0.55	20 (300)
$8V/TiO_2$	7.82	25.7	36	19.3	31	230	0.70	55 (300)

Figure 01

Click here to download high resolution image

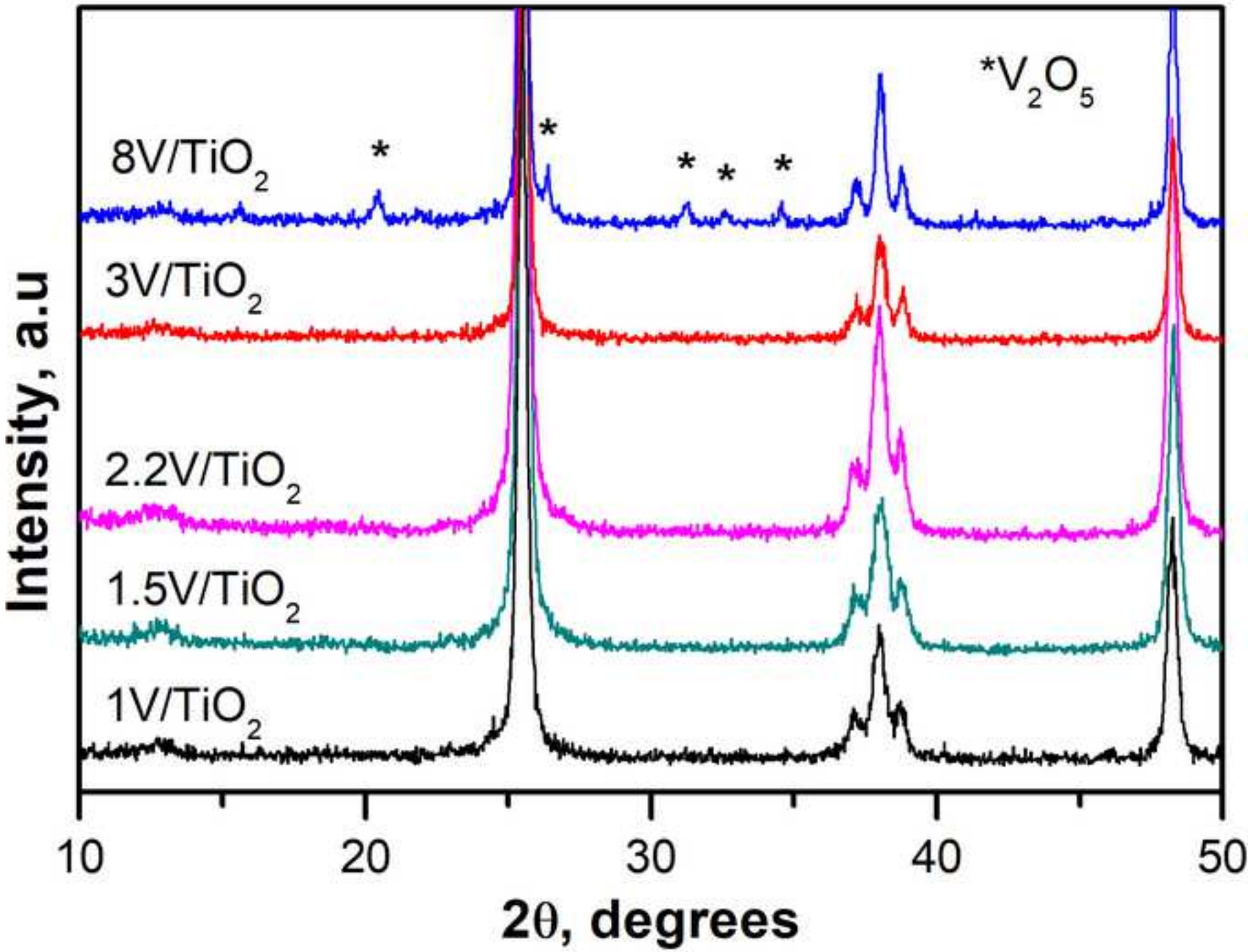

Figure 02

Click here to download high resolution image

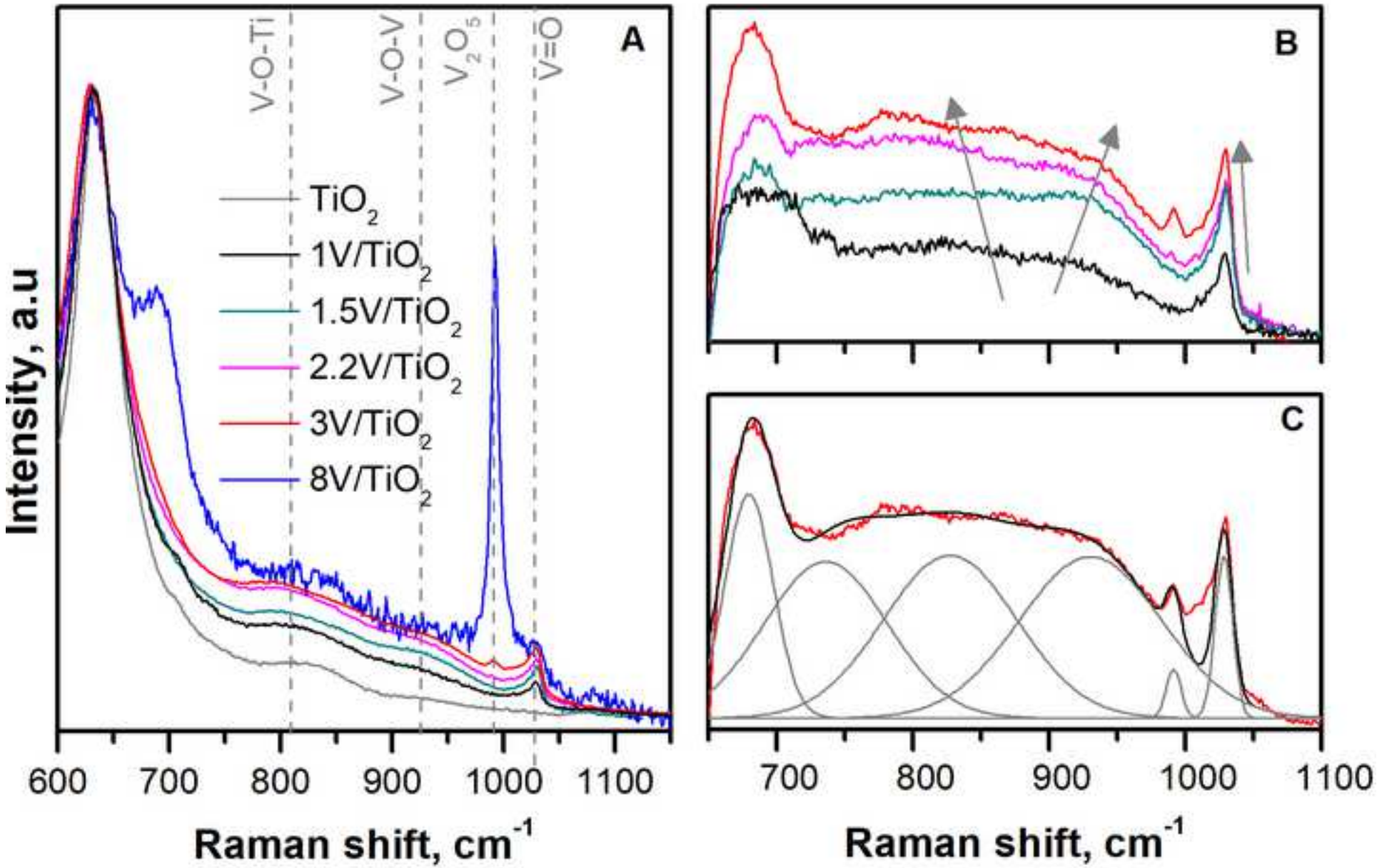

Figure 03
Click here to download high resolution image

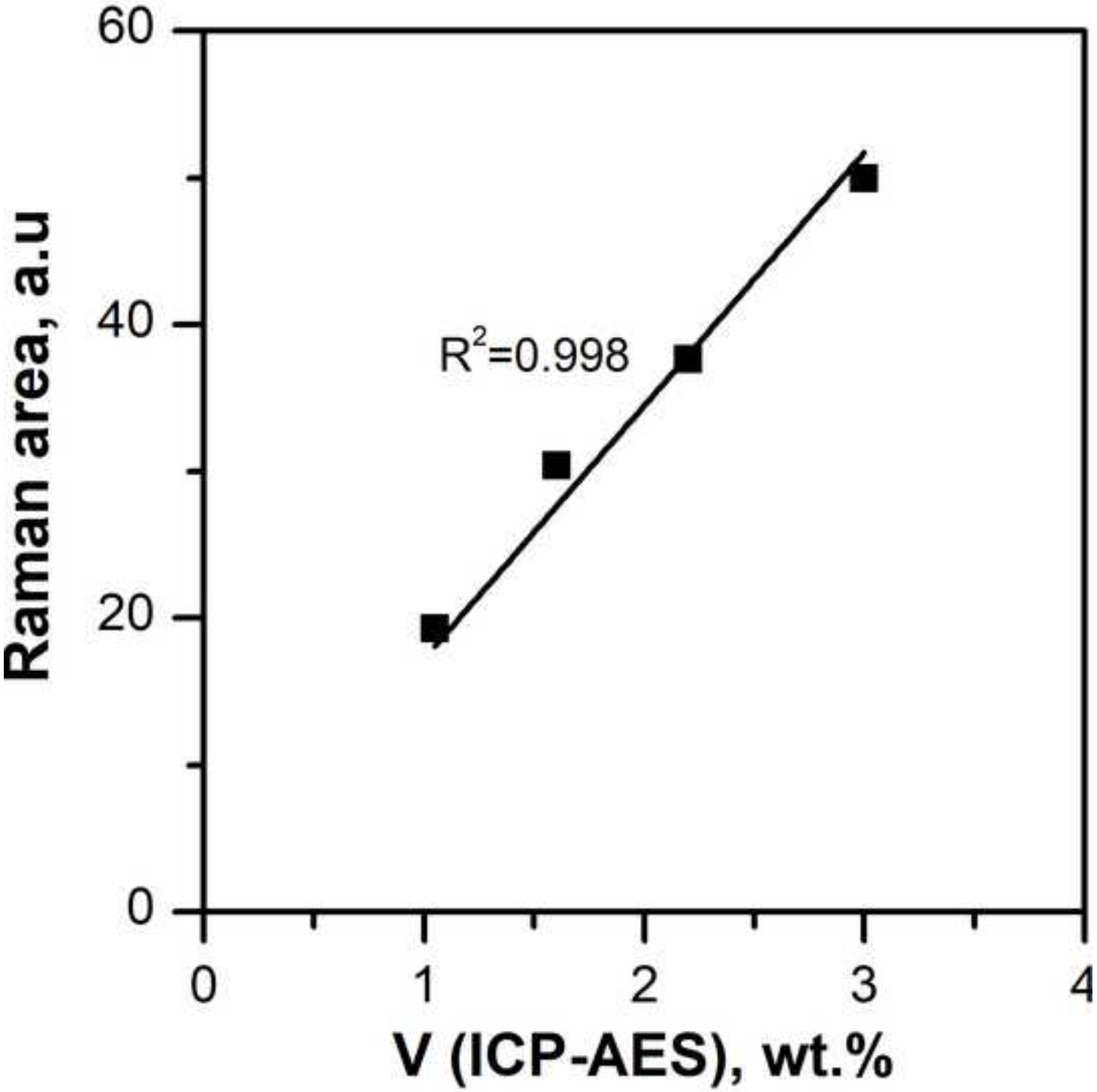

Figure 04

Click here to download high resolution image

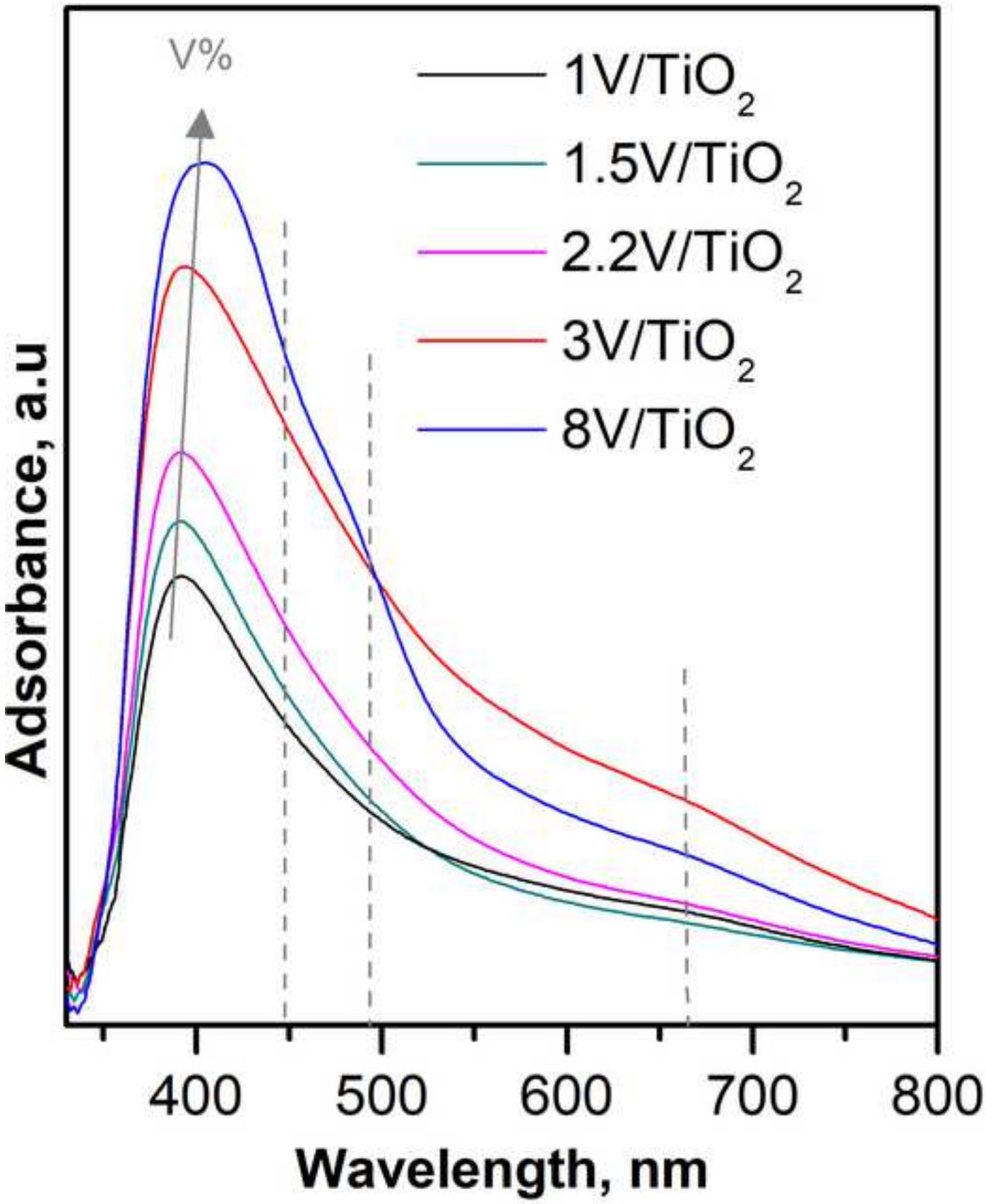

Figure 05

Click here to download high resolution image

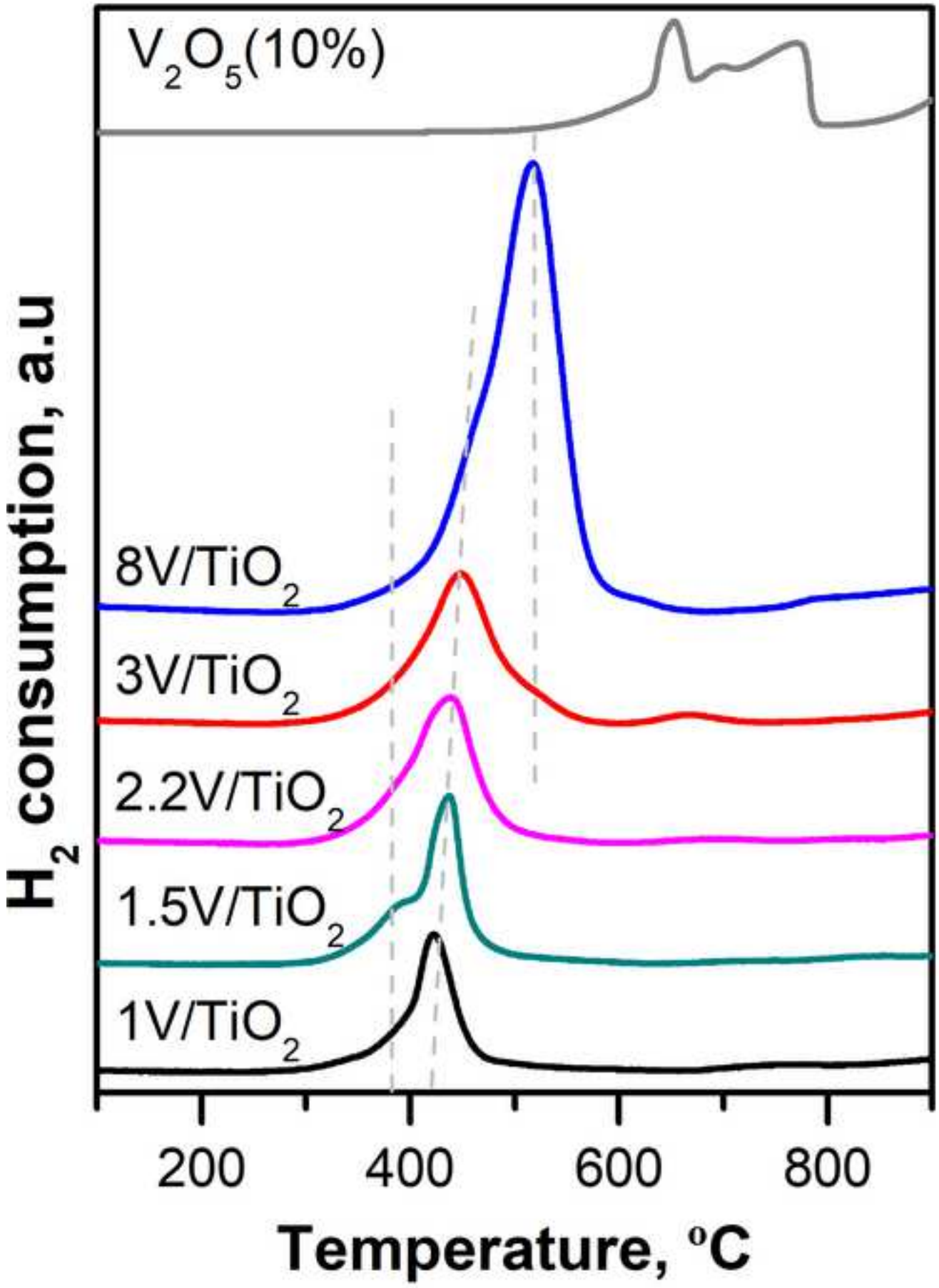

Figure 06

Click here to download high resolution image

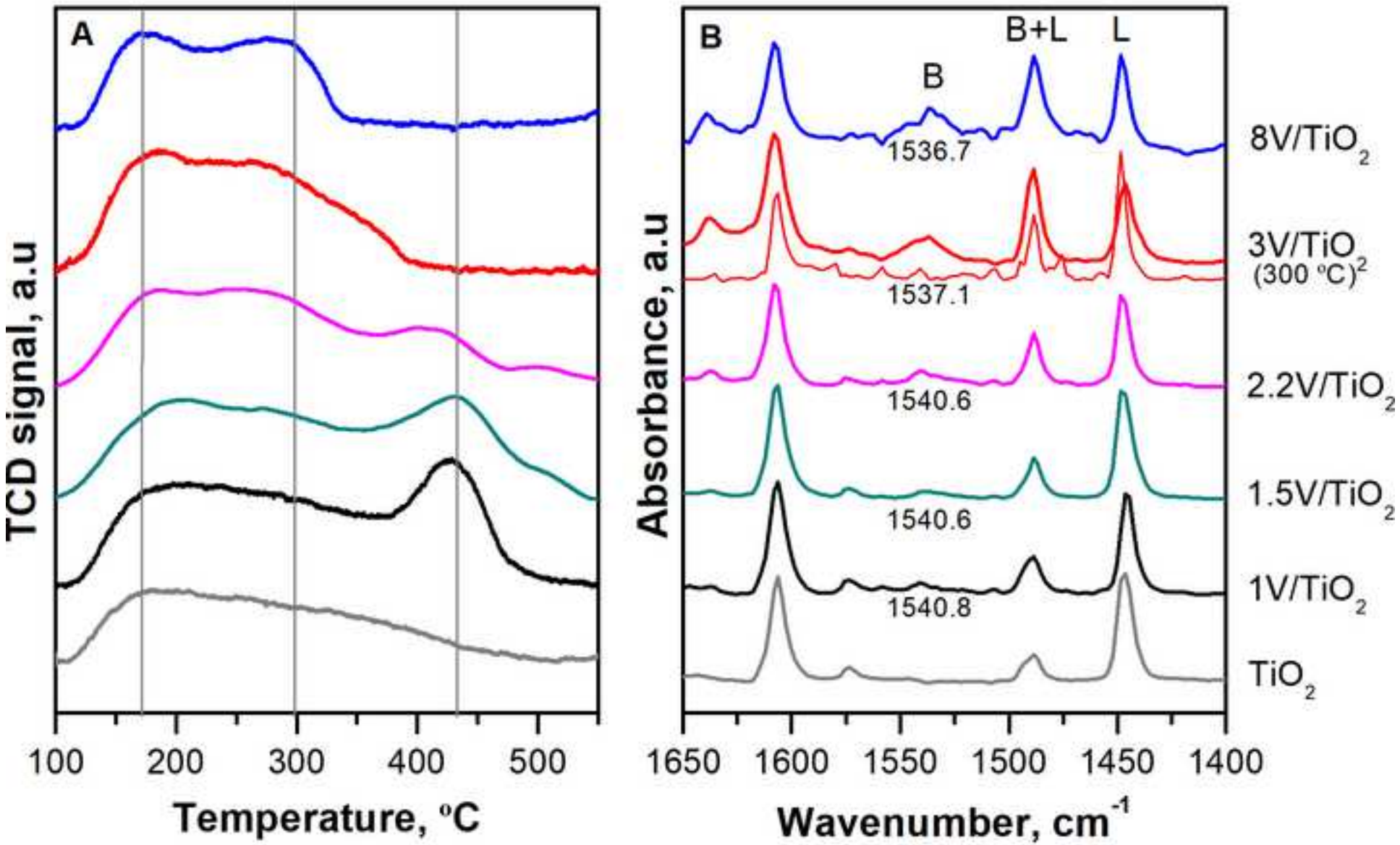

Figure 07

Click here to download high resolution image

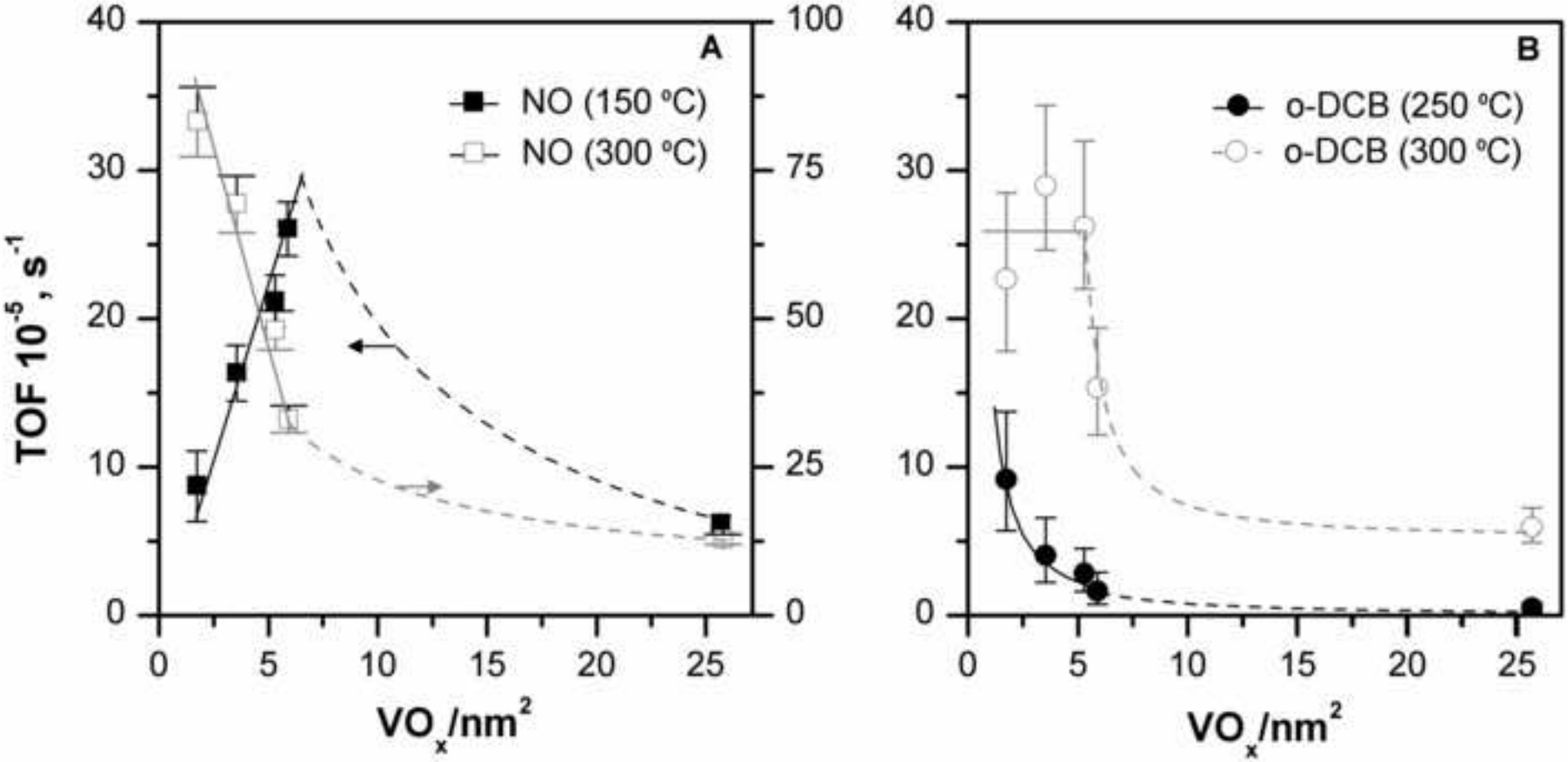

Figure 08

Click here to download high resolution image

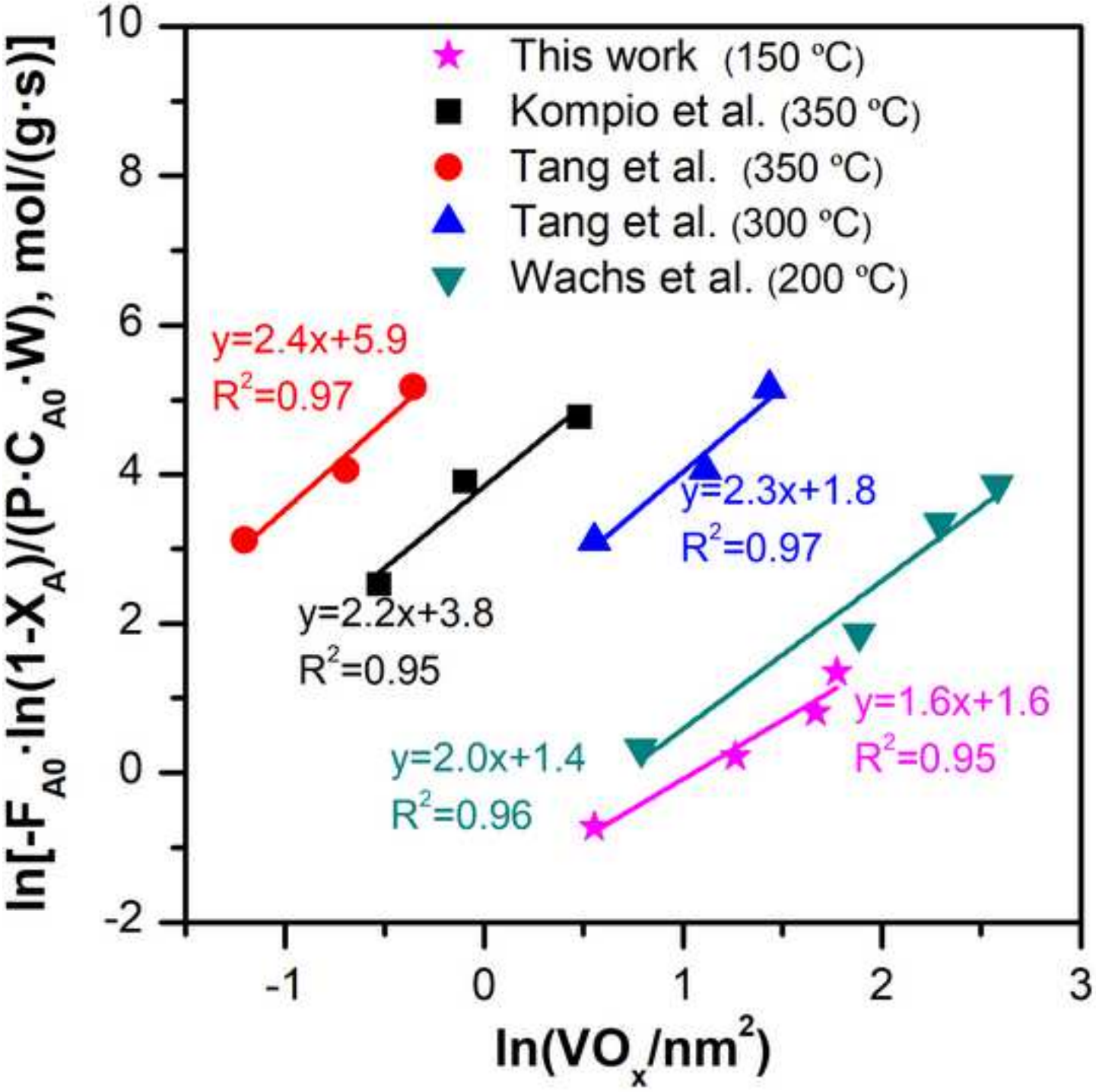

Figure 09

Click here to download high resolution image

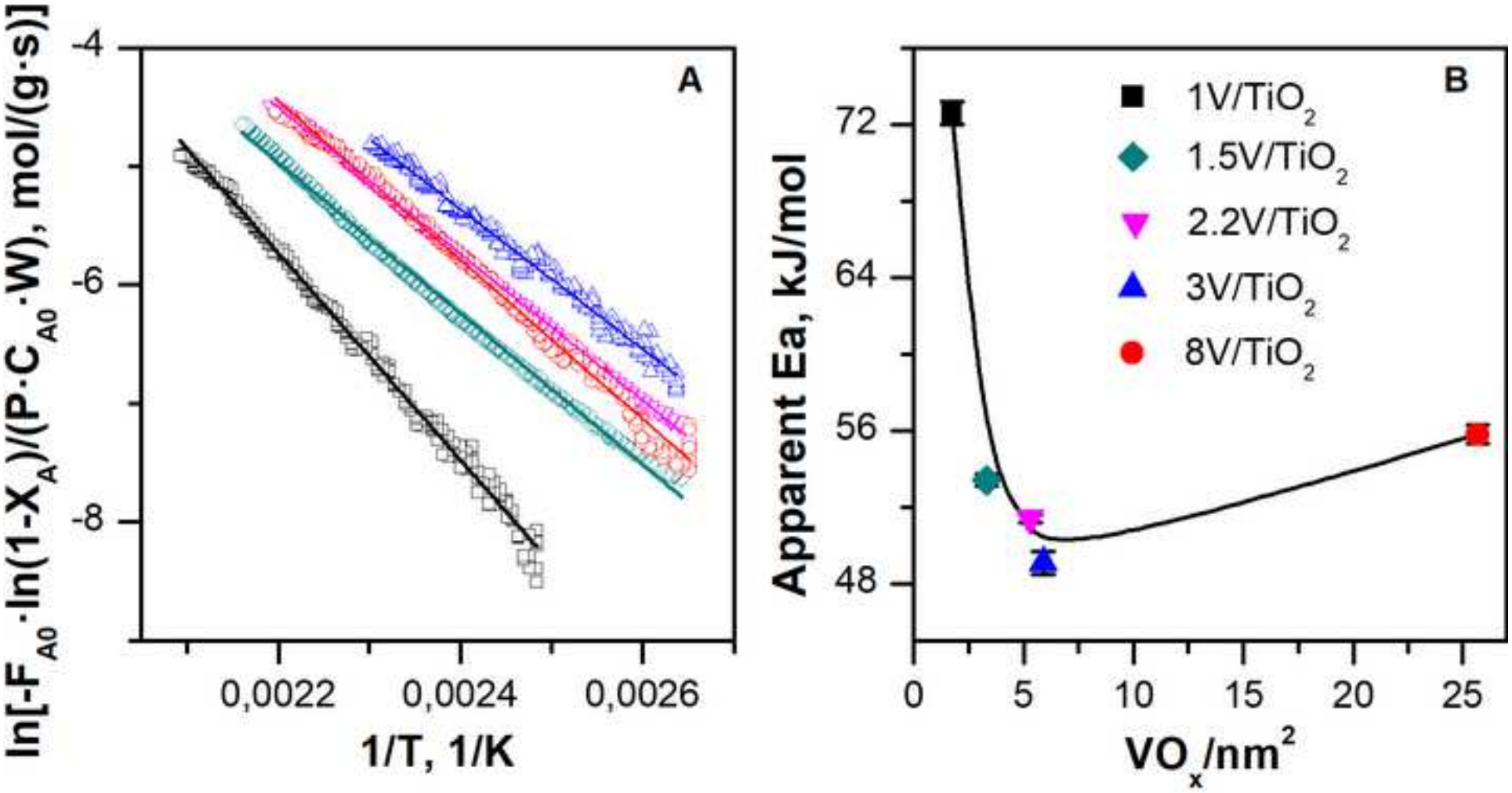

Figure 10

Click here to download high resolution image

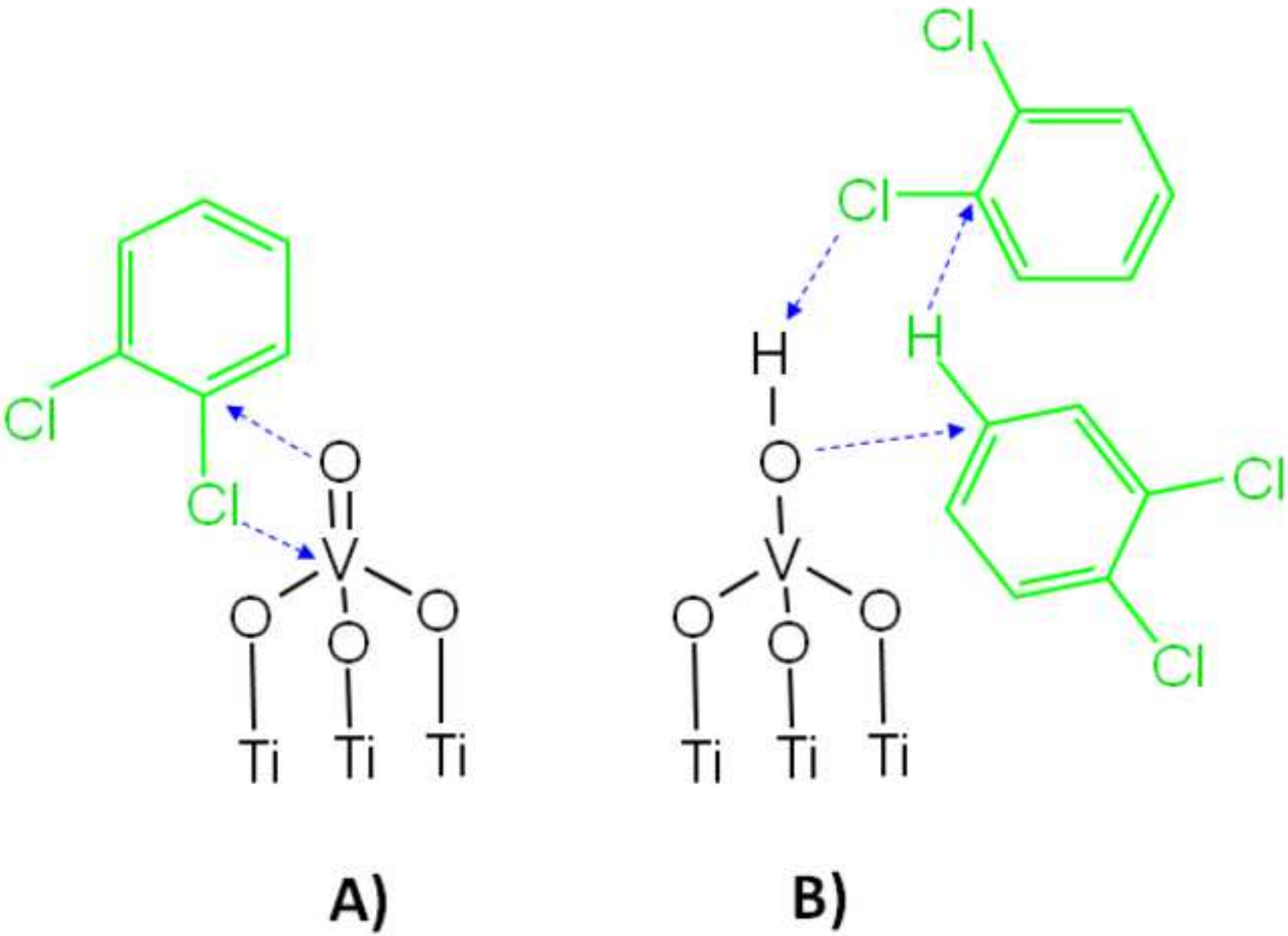

Figure 11

Click here to download high resolution image

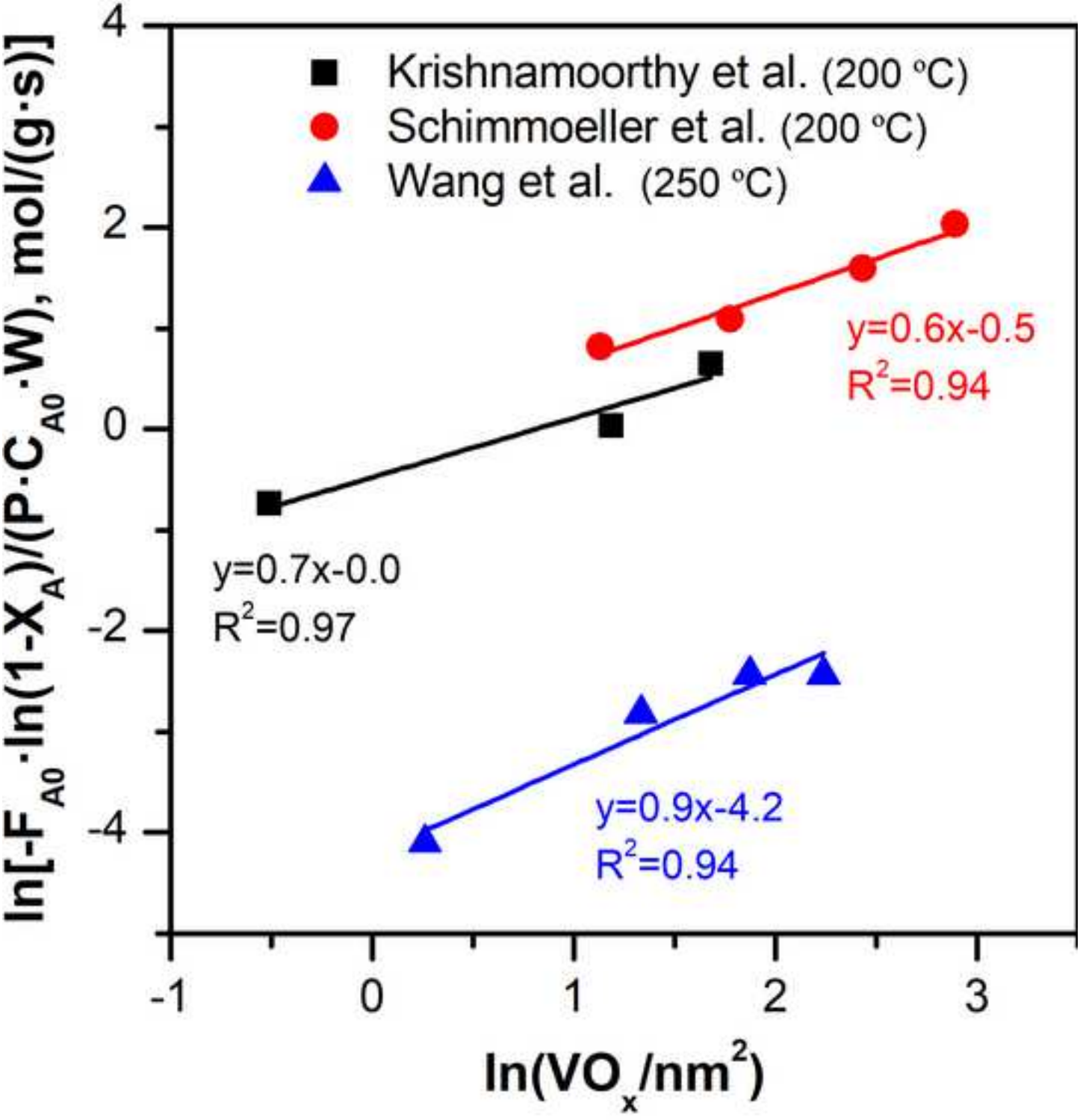

Figure 12

Click here to download high resolution image

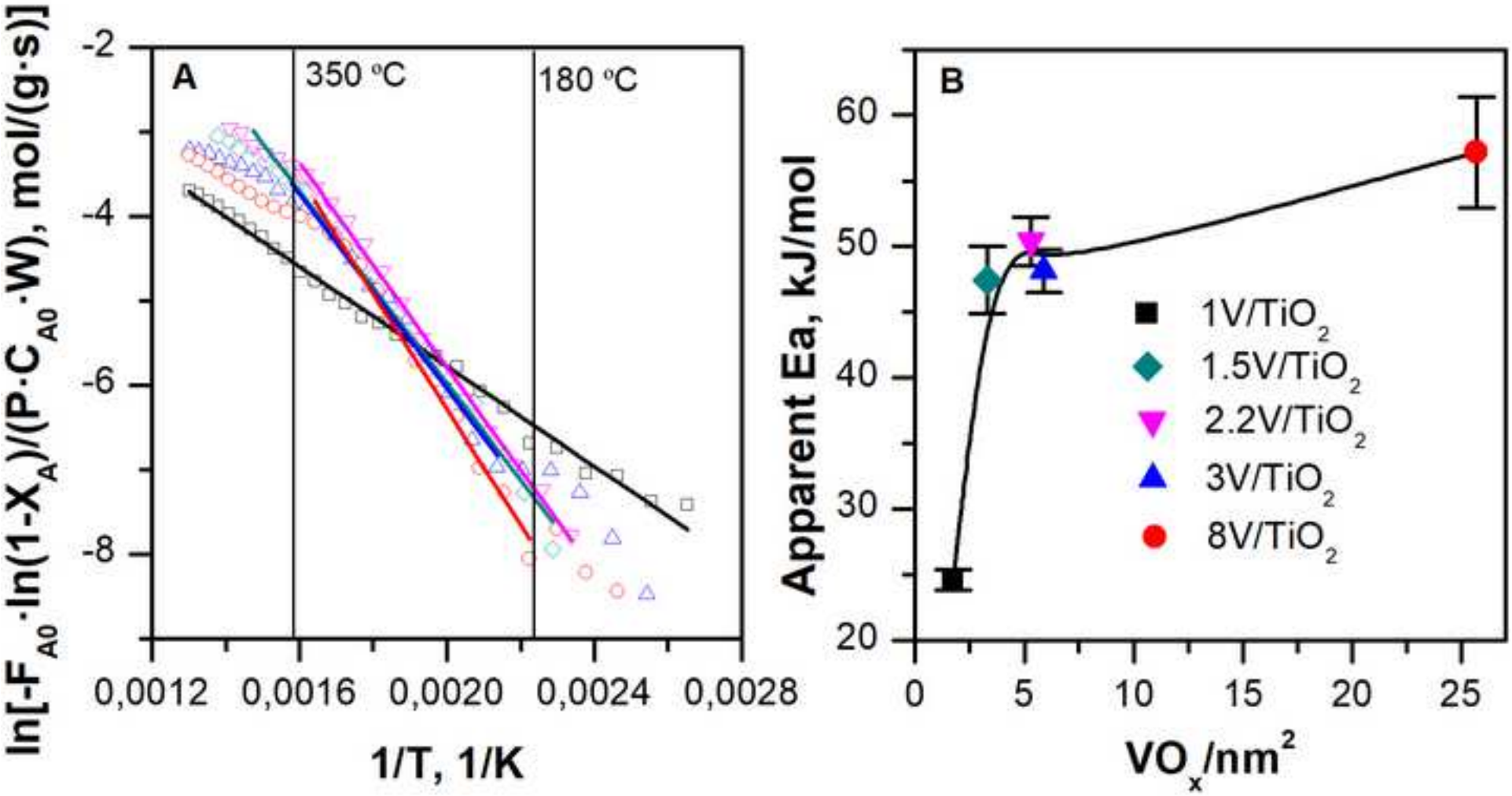

Figure 13

Click here to download high resolution image